

Terrain Trapped Airflows and Precipitation Variability during an Atmospheric River Event^o

JU-MEE RYOO,^{a,b,c} SEN CHIAO,^c J. RYAN SPACKMAN,^a LAURA T. IRACI,^a F. MARTIN RALPH,^d ANDREW MARTIN,^d RANDALL M. DOLE,^{e,f} JOSETTE E. MARRERO,^{a,g,h} EMMA L. YATES,^{a,g} T. PAUL BUI,^a JONATHAN M. DEAN-DAY,^{a,g} AND CECILIA S. CHANG^{a,g}

^a *Earth Science Division, NASA Ames Research Center, Moffett Field, California*

^b *Science and Technology Corporation, Moffett Field, California*

^c *San José State University, San Jose, California*

^d *Center for Western Weather and Water Extremes, Scripps Institution of Oceanography, University of California, San Diego, La Jolla, California*

^e *CIRES, University of Colorado Boulder, Boulder, Colorado*

^f *NOAA/Earth System Research Laboratory, Boulder, Colorado*

^g *Bay Area Environmental Research Institute, Moffett Field, California*

(Manuscript received 16 February 2019, in final form 29 December 2019)

ABSTRACT

We examine thermodynamic and kinematic structures of terrain trapped airflows (TTAs) during an atmospheric river (AR) event impacting Northern California 10–11 March 2016 using Alpha Jet Atmospheric eXperiment (AJAX) aircraft data, in situ observations, and Weather and Research Forecasting (WRF) Model simulations. TTAs are identified by locally intensified low-level winds flowing parallel to the coastal ranges and having maxima over the near-coastal waters. Multiple mechanisms can produce TTAs, including terrain blocking and gap flows. The changes in winds can significantly alter the distribution, timing, and intensity of precipitation. We show here how different mechanisms producing TTAs evolve during this event and influence local precipitation variations. Three different periods are identified from the time-varying wind fields. During period 1 (P1), a TTA develops during synoptic-scale onshore flow that backs to southerly flow near the coast. This TTA occurs when the Froude number (Fr) is less than 1, suggesting low-level terrain blocking is the primary mechanism. During period 2 (P2), a Petaluma offshore gap flow develops, with flows turning parallel to the coast offshore and with $Fr > 1$. Periods P1 and P2 are associated with slightly more coastal than mountain precipitation. In period 3 (P3), the gap flow initiated during P2 merges with a pre-cold-frontal low-level jet (LLJ) and enhanced precipitation shifts to higher mountain regions. Dynamical mixing also becomes more important as the TTA becomes confluent with the approaching LLJ. The different mechanisms producing TTAs and their effects on precipitation pose challenges to observational and modeling systems needed to improve forecasts and early warnings of AR events.

1. Introduction

Extreme precipitation events have become more frequent and intense in recent years in California (Dettinger 2011). These events can cause hazardous and costly

flooding impacts, but also contribute substantially to essential local water resources. Deleterious impacts were recently exemplified in California over the period of November 2016–March 2017, when numerous extreme precipitation events resulted in severe flooding. Along the U.S. West Coast, such extreme events often occur in conjunction with landfalling atmospheric rivers (ARs), which are characterized by elongated, deep, and narrow corridors of concentrated water vapor transport that form in the warm sector of extratropical cyclones (Zhu and Newell 1994, 1998; Ralph et al. 2004, 2005a, 2006; Neiman et al. 2008; Dettinger 2011; Dettinger et al. 2011; Guan et al. 2013; Ryoo et al. 2015). As ARs impinge upon the mountainous terrain along the west

^o Supplemental information related to this paper is available at the Journals Online website: <https://doi.org/10.1175/JHM-D-19-0040.s1>.

^h Current affiliation: Sonoma Technology, Petaluma, California.

Corresponding author: Ju-Mee Ryoo, ju-mee.ryoo@nasa.gov

coast, heavy precipitation can be generated by orographic lifting of moist air on the windward slopes of the mountains and intensified further by convergence and vertical motions resulting from subsynoptic interactions with terrain trapped airflows (TTAs) flowing parallel to the coastal ranges.

Terrain blocking is one mechanism for forming a TTA, with high static stability conducive to onshore flow turning parallel to rather than over higher terrain. The local blocking decelerates the flow, with pressure rises along the windward slopes. To balance the pressure gradient force normal to the barrier and the Coriolis force, the local disruption of the force balance (i.e., geostrophic wind) leads to ageostrophic acceleration parallel to the barrier, resulting in a barrier jet (BJ), (Loescher et al. 2006). Pierrehumbert and Wyman (1985) found that the low-level terrain blocked flow often contains a BJ oriented parallel to the long axis of the high mountain range, which is maintained by a statically stable pressure ridge on the windward slope. Through modeling and a Froude number (Fr) analysis, where $Fr = U/Nh$ with U the barrier-normal wind speed, h the barrier height, and N the Brunt–Väisälä frequency, Kim and Kang (2007) showed the low-level water vapor transport by a BJ in a low- Fr regime ($Fr < 1$) accelerates northward moisture transport, resulting in a strong meridional precipitation gradient over the Sierra Nevada. More recently, Neiman et al. (2013) found that the Sierra barrier jets (SBJs) reach their maximum intensity during the strongest AR flow aloft, and that inland penetration of the AR through the San Francisco Bay gap in the coastal mountains maintains moist air transport by the SBJ. BJs due to low-level blocking are commonly observed with mountain ranges, including the Rocky Mountains (Colle and Mass 1995), the Sierra Nevada (Parish 1982; Neiman et al. 2010, 2013, 2014), the coastal mountains of California (Doyle and Warner 1993; Doyle 1997; Yu and Smull 2000), the Appalachians (Bell and Bosart 1988), the European Alps (Chen and Smith 1987), and the Alaskan coast (Olson et al. 2007).

TTAs can also form through mechanisms other than terrain blocking, such as with gap flows (Loescher et al. 2006; Valenzuela and Kingsmill 2015). Gap flows may develop when significant pressure and temperature differences are present between the entrance and exit of a low-elevation gap in a mountain range, leading to a local force imbalance and ageostrophic flow through the gap that often extends well beyond the gap exit. Using a mesoscale model, Steenburgh et al. (1998) examined a gap flow through a low-elevation gap in the Sierra Madre over the Gulf of Tehuantepec during a Central American cold surge event (e.g., 12–14 March 1993). The flow reached its maximum speed at the surface of $\sim 25 \text{ m s}^{-1}$ offshore. Upon exiting the gap, the locally

unbalanced flow turns anticyclonically due to the Coriolis force, becoming parallel to the terrain axis (Valenzuela and Kingsmill 2017).

TTAs associated with gap flows and their relationship to orographic precipitation over California have been examined in previous observational studies (Neiman et al. 2006; Valenzuela and Kingsmill 2015, 2017). Neiman et al. (2006) identified relationships between Petaluma gap flow and rainfall over Bodega Bay in California using 915-MHz wind profiler observations during winter storms from 1997 to 2004. They found that rain rates and total rainfall increased over Bodega Bay in strong gap flow cases, and suggested that further understanding of relationships between the terrain-modulated flows and precipitation was needed to help improve forecasts. Using Doppler radar, Valenzuela and Kingsmill (2015) found that TTAs forced by the Petaluma gap flow enhanced precipitation over the ocean and near the coast. They demonstrated how TTAs could combine with pre-cold-frontal low-level jets (LLJs). These pre-cold-frontal LLJs are subsynoptic scale features occurring within many extratropical cyclones, and are characterized by relatively warm temperatures, weak stratification, high water vapor content, and strong low-altitude winds (Browning and Pardoe 1973; Ralph et al. 2005a). In the Valenzuela and Kingsmill (2015) study, profile sounding data, while of great value, was limited to observations at single points. Thus, these observations could not determine whether mixing was occurring at the pre-cold-frontal LLJs and TTA interface or interactions with the synoptic LLJ and topography. Such questions motivated us to augment the new observations reported in this study with dynamical diagnostic analyses and regional model simulations.

Prior modeling studies have helped greatly to clarify the fundamental connections between subsynoptic low-level jets, orographically modified flows, and precipitation, as well as to reveal gaps in our current understanding, observations, and modeling capabilities. Doyle (1997) showed for a storm system impacting the northern California coast in January 1995 that the mesoscale precipitation structure was simulated reasonably well, but with a slight discrepancy between the observed and the simulated orientation of the frontal rainband. Using the high-resolution fifth-generation Pennsylvania State University–National Center for Atmospheric Research (NCAR) Mesoscale Model (MM5; Grell et al. 1994), Olson et al. (2007) also showed that the model simulation adequately reproduced the southeastern Alaskan coastal jets, low-level pressure perturbations, and orographic flow response, but had a timing bias associated with the approach of a pressure trough, and a magnitude bias for precipitation. Ongoing questions related to understanding

and modeling precipitation timing, magnitude, and location are vital to improving early warnings and forecasting impacts, helping to motivate the research reported here.

Here, we first examine mechanisms for the formation of TTAs and associated changes in wind fields over Northern California during an AR event occurring over the period of 10–11 March 2016. Both observational and modeling approaches are employed, including aircraft observations, surface wind profiler observations, reanalysis data, and a high-resolution (1-km) Advanced Research version of the Weather Research and Forecasting (WRF-ARW) Model simulation. Temporal and spatial variations in winds and precipitation are also examined, and they are related to the different mechanisms for TTA formation and large-scale mixing during the AR event. Our central hypothesis is that wind speed and direction are closely related to different processes of TTA formation and that these differences have discernible impacts on the location and intensity of precipitation during an AR event. We evaluate this hypothesis by comparing observations with model simulations and performing diagnostic analyses of stability, force balance, and dynamical mixing relationships during the evolution of this AR event.

The following section provides details on the experimental design, observational and model data, and methods used in this study for an AR case that impacted the northern and central California coast on 10–11 March 2016. Subsequent sections then describe observations of TTAs, their relationships to time-varying synoptic and precipitation features, and comparisons with model results. The last section summarizes primary findings and implications from this study.

2. Experimental design

a. Airborne instrumentation and flight plan

To map out the structure and gradients of water vapor and wind in the mid- and low troposphere in the coastal region south of San Francisco Bay, in situ measurements of water vapor and 3D winds were collected during a flight originating from Moffett Field, California (37.42°N , 122.05°W). The aircraft performed six consecutive level flight legs (see Figs. 1 and 3) between 1450 and 1605 Pacific standard time (PST) 10 March 2016 (from 2250 UTC through 0005 UTC; AJAX flight 181). Offshore level legs were executed at multiple altitudes (0.03, 0.2, 1.2, 2.4, and 3.1 km), paralleling the coast from as far north as conditions allowed at each altitude and continuing in a straight line to the southeast, extending nearly to Pt. Sur, California. The final leg was executed closer to shore, spanning the mouth of Monterey Bay and

then paralleling the original flight line but closer to shore. Water vapor volume mixing ratio is measured with a commercial instrument employing cavity ringdown spectroscopy (CRDS) and data for the flight reported here. H_2O is estimated to have an uncertainty of <4%–6%, depending on the amount of water vapor present (Filges et al. 2015). For this study, these values are converted into H_2O mass (g kg^{-1}) mixing ratios.

As part of the Alpha Jet Atmospheric eXperiment (AJAX), the Meteorological Measurement System (MMS; Scott et al. 1990; Gaines et al. 1992) provided high-resolution pressure, temperature, and 3D (u , v , and w) wind measurements. This instrument consists of three major systems: 1) an air motion sensing system to measure the air velocity with respect to the aircraft, 2) an aircraft motion sensing system to measure the aircraft velocity with respect to the earth surface, and 3) a data acquisition system to sample, process, and record the measured quantities. Further details of the complete airborne facility are presented in Hamill et al. (2016).

b. Other instrumentation and datasets

National Oceanic and Atmospheric Administration (NOAA) 449-MHz surface wind profiler data collected at the Bodega Bay, California (BBY, 38.3°N , 123.1°W , elevation 15 m), site were used in this study. This radar wind profiler detects a Doppler shift due to air motion to obtain wind speeds and directions from 180 m above the ground surface up to 8 km, depending on atmospheric conditions. Together with this, the Global Positioning System Meteorology (GPS-Met), a ground-based water vapor observing system measuring atmospheric total-column integrated precipitable water vapor, is collocated with the existing Hydrometeorology Testbed (Ralph et al. 2005b; HMT-West) wind profiler at the BBY site (White et al. 2013). At BBY (coastal), additional hourly observations of integrated water vapor, total wind speed, wind direction, total integrated water vapor flux, upslope wind speed and direction, and upslope integrated water vapor (IWV) flux were provided by the NOAA Physical Science Division (PSD) (<https://www.esrl.noaa.gov/psd/data/obs/datadisplay/>). Coastal precipitation (at BBY) and mountain precipitation [at Cazadero, California (CZD), 38.6°N , 123.2°W , elevation 478 m] data from tipping-bucket measurements (White et al. 2013) were also provided by NOAA PSD. Since IWV fluxes are closely linked to orographic precipitation (Neiman et al. 2002), we used the upslope IWV fluxes to show the strength of the water vapor fluxes orthogonal to the axis of the coastal mountains and examine relationships to temporal precipitation variability over coastal and mountainous regions during the course of the AR event.

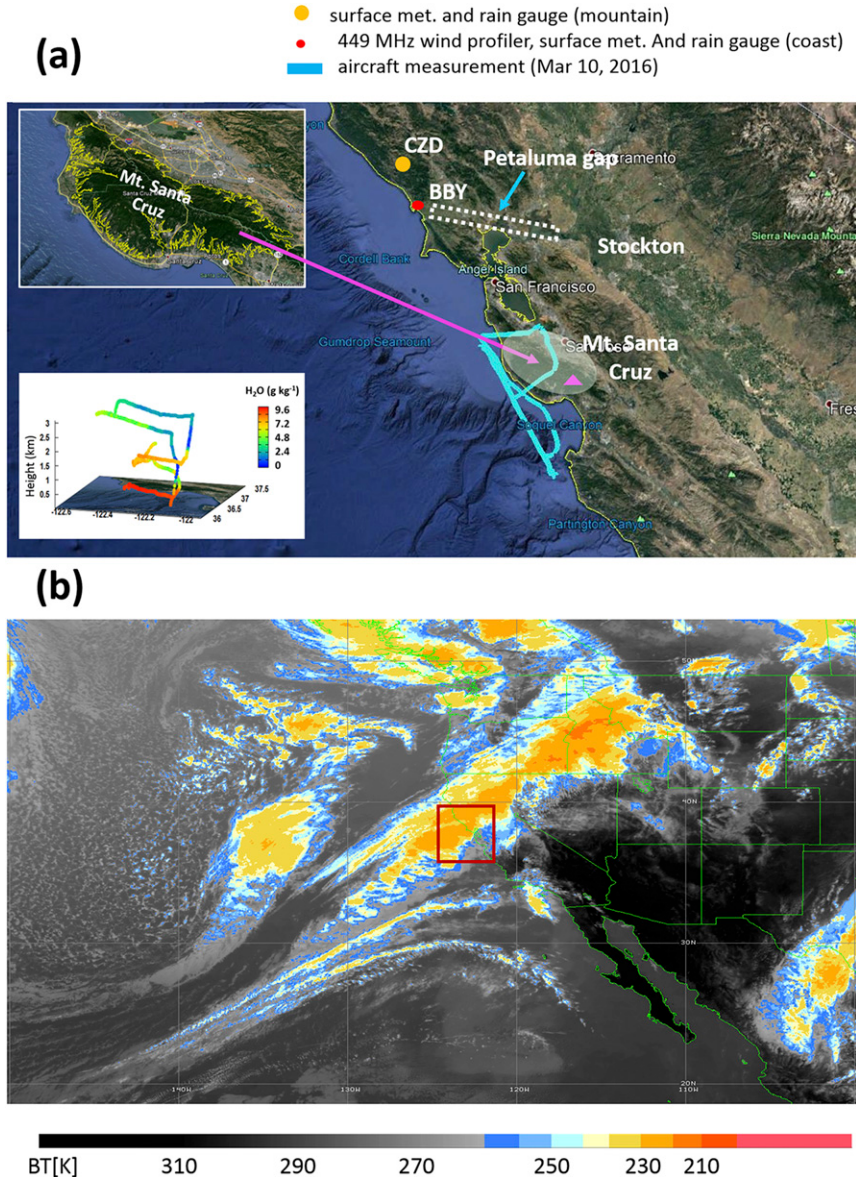


FIG. 1. (a) Map of the study region overlaid with observing systems. The legend identifies the coastal (BBY) and mountain (CZD) measurement sites. The inset shows a 3D view of water vapor mixing ratio (g kg^{-1}) measured by the Alpha Jet Atmospheric eXperiment (AJAX) flight from 2250 UTC 10 Mar to 0005 UTC 11 Mar 2016. (b) Satellite image of 10.7- μm brightness temperature (in color) obtained from NASA Langley Cloud and Radiation Research [from *Geostationary Operational Environmental Satellite-15 (GOES-15)* imagery and cloud products] at 2230 UTC 10 Mar 2016. The red box indicates the area expanded in (a). The green area with the yellow line represents the Santa Cruz mountains (Mt. Santa Cruz) area. The magenta triangle represents the peak of Mt. Santa Cruz.

MERRA-2 reanalyses were used for constructing synoptic-scale analysis and diagnostic fields during the AR event. MERRA-2 is a NASA atmospheric reanalysis for the satellite era using the Goddard Earth Observing System Model, Version 5 (GEOS-5) with its Atmospheric Data Assimilation System (ADAS), version 5.12.4.

The MERRA-2 horizontal winds (u , v), vertical wind (ω), and temperatures are reported at a horizontal resolution of 0.66° longitude $\times 0.5^\circ$ latitude on 42 pressure levels spanning from 1000 to 0.01 hPa, at 3-hourly time resolution. See [Bosilovich et al. \(2016\)](#) for further details regarding the MERRA-2 reanalyses.

c. Model simulations

All model simulations here were conducted with the WRF-ARW Model version 3.8. (Skamarock et al. 2008). Prior studies have used the WRF-ARW to investigate atmospheric river events over Northern California (Eiserloh and Chiao 2015; Martin et al. 2018). Eiserloh and Chiao (2015) showed that this model was able to reproduce well monthly precipitation and snowfall over this region. Initial and time-dependent lateral boundary conditions were supplied from NCEP North American Mesoscale Forecast System (NAM) analyses at 12-km horizontal resolution. The simulation was initialized at 1200 UTC 9 March 2016 and run for 72 h until the end of the AR event at 1200 UTC 12 March. The selected horizontal grid spacing was 1 km, with 41 vertical levels. The Thompson graupel (2-moment) micro-physics scheme (Thompson et al. 2004) and the Yonsei University (YSU) boundary layer microphysics scheme (Hong et al. 2006) were used. The Thompson scheme was chosen because it has been shown to produce a smaller wet bias in cold season quantitative precipitation forecasting (QPF) over portions of northern California than other popular microphysics schemes in WRF (Jankov et al. 2007). The Noah land surface model (Ek et al. 2003), the Goddard scheme for shortwave radiation (Chou and Suarez 1994), and the Rapid Radiative Transfer Model (RRTM) scheme for longwave radiation (Mlawer et al. 1997) were also employed.

A Q diagnostic was used as a measure of the relative contribution of strain and rotation in the large-scale flow to identify whether the horizontal dynamical mixing may be significant. Here,

$$Q = \frac{1}{2} \left(\frac{1}{\cos \varphi} \frac{\partial u}{\partial \lambda} - v \tan \varphi \right)^2 + \frac{1}{2} \left(\frac{\partial v}{\partial \varphi} \right)^2 + \frac{\partial u}{\partial \varphi} \left(\frac{1}{\cos \varphi} \frac{\partial v}{\partial \lambda} + u \tan \varphi \right), \quad (2)$$

where λ and φ are longitude and latitude, respectively (Haynes 1990; Fairlie et al. 2007). This measure has been used in studies of intermediate to small-scale variability in the troposphere to examine dynamical mixing, such as during upper-level Rossby wave breaking in the upper troposphere. Here large positive Q values suggest increased strain with enhanced mixing, while small and negative Q values indicate dominance of rotation of the flow with reduced mixing.

d. Locations of measurements, flight track, and AR event

Figure 1a shows a map of the study region and the AJAX flight track for the AR event on 10 March 2016.

The map also identifies the wind profiler site (BBY), the mountain precipitation site (CZD), and the Petaluma gap. The inset plot shows the spatial variability of water vapor in the offshore region measured from the aircraft. Aircraft data were collected from the surface to ~ 3.1 km (~ 10 kft). Level leg flight data show that water vapor is higher at low altitudes than at higher altitudes. A similar flight to the north of San Francisco Bay was performed on 9 December 2015, but the lower level legs were limited by flight constraints of reduced visibility and air traffic control restrictions, with no TTAs features found (not shown).

Bands of low brightness temperature in satellite imagery (Fig. 1b), suggestive of deep convective clouds and surface rainfall show the signature of an AR event (Galewsky and Sobel 2005) extending from the eastern Pacific to the western United States. Based on the IIV and integrated water vapor flux (IVT) computed from MERRA-2, this event meets the three quantitative detection criteria for defining an AR: 1) IVT $> 500 \text{ kg m}^{-1} \text{s}^{-1}$, 2) width $< 1000 \text{ km}$, and 3) length $> 1500 \text{ km}$, where IVT is computed as $\text{IVT} = (1/g) \int_0^p q \mathbf{U} dp$, with g the acceleration of gravity, q the specific humidity, $\mathbf{U} = (u, v)$ the horizontal wind, and p the pressure, with the integration performed over the pressure levels from 1000 to 300 hPa. Similar evaluations performed with the NCEP reanalysis (Rutz et al. 2014) and Global Forecast System (GFS) model (Wick et al. 2013a,b) were consistent in identifying this event as satisfying the AR criteria.

3. Synoptic conditions and the observed characteristics of the TTA

Lower-tropospheric wind maxima that are often observed in the coastal zone can be enhanced by coastal orography due to BJs (Bell and Bosart 1988; Doyle and Warner 1993; Doyle 1997). TTAs can be forced by either onshore or offshore flow at the coast at various altitudes (Doyle 1997; Olson et al. 2007; Valenzuela and Kingsmill 2015). To examine how a specific synoptic condition can provide favorable conditions for generating a TTA and how the flow evolves during an AR event, we first provide a synoptic overview for this AR event.

a. Synoptic conditions

Figure 2 shows the evolution of specific humidity q , horizontal wind, temperature T at 700 hPa, sea level pressure, and potential vorticity (PV) at 500 hPa for the AR period of 10–11 March 2016 using MERRA-2 reanalysis data. As the AR approaches the western U.S., a robust upper-level trough associated with high PV [> 1 potential vorticity units (PVU); $1 \text{ PVU} = 10^{-6} \text{ K kg}^{-1} \text{ m}^2 \text{ s}^{-1}$] at 500 hPa is located offshore near the coast of California. In advance of this system, strong low-level southerlies and

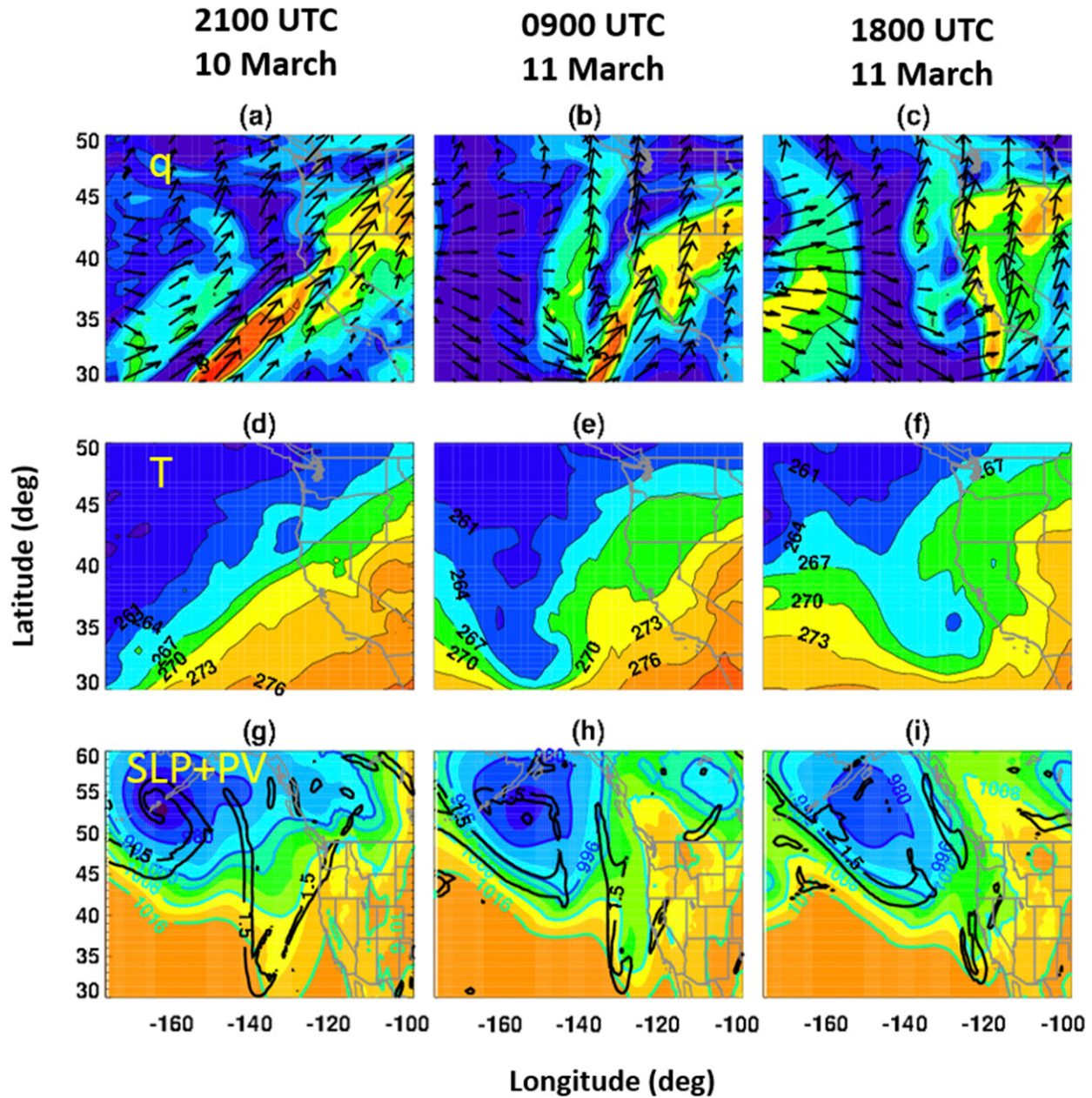


FIG. 2. Longitude–latitude cross section of (a)–(c) water vapor mixing ratio (g kg^{-1}) overlaid by horizontal wind vectors (m s^{-1}) at 700 hPa; (d)–(f) temperature (K) at 700 hPa; and (g)–(i) sea level pressure (hPa; in color) overlaid by potential vorticity (PV) at 500 hPa where PVU = 1.5 at (left) 2100 UTC 10 Mar, (center) 0900 UTC 11 Mar, and (right) 1800 UTC 11 Mar 2016 obtained from the MERRA-2 reanalysis data.

southwesterlies are present over the coast of California with relatively dry airmass. The advancing deep trough is similar to the synoptic situation described by Colle et al. (2006), who found that cold season BJs are associated with an anomalously deep large-scale upper-level trough approaching the coast. Similar features are found at 850 hPa (not shown). By 2100 UTC 10 March, the high and narrow water vapor band is elongated

from southwest to northeast with strong southwesterlies and relatively warmer temperature inland (Figs. 2a,d) compared to later in the event. At the surface, low pressure is centered over the eastern North Pacific, with southwesterly flow extending toward the California coast (Fig. 2g). PV in the deep upper trough has values exceeding 1.5 PVU, suggesting that of the dynamical tropopause extends downward to at least 500 hPa.

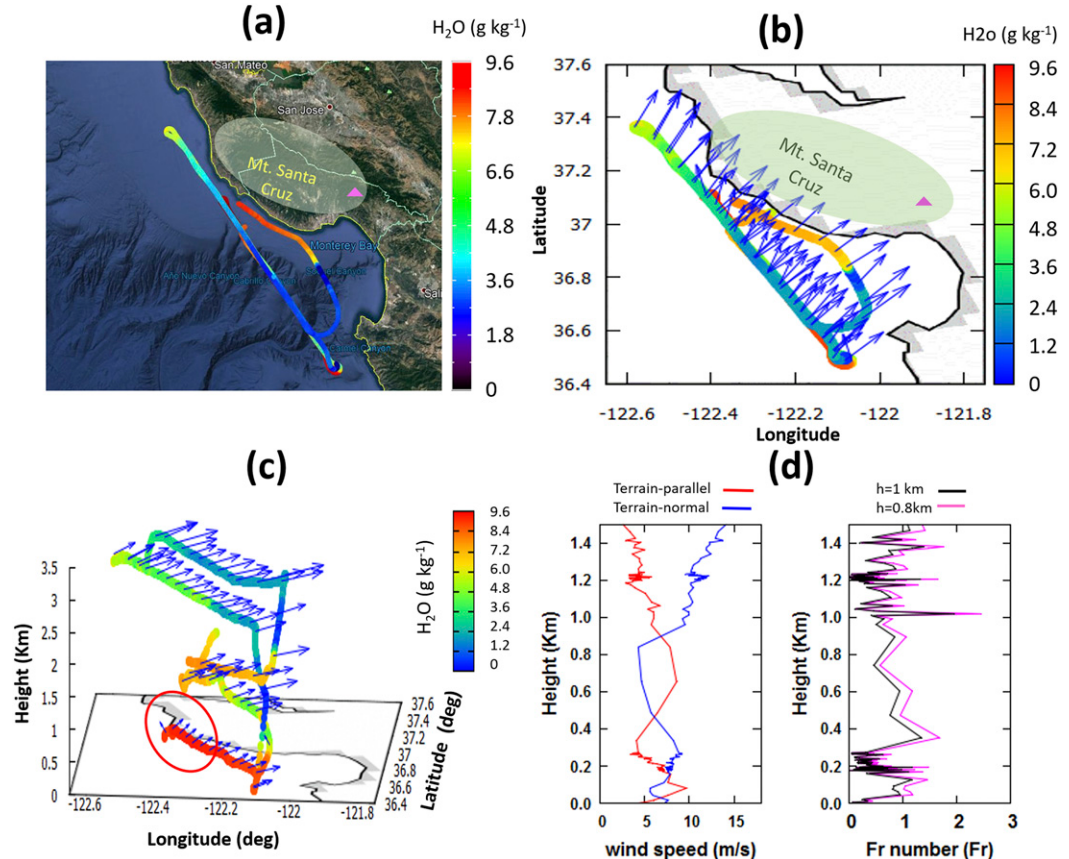


FIG. 3. Maps of (a) measured water vapor and (b) wind along the AJAX flight track. (c) Water vapor mixing ratio (g kg^{-1}) overlaid with horizontal wind vectors (m s^{-1} ; blue) measured by the AJAX flight. The red circle indicates the deflected flow toward the coast along the transect from SE to NW. (d) The vertical profiles of terrain-parallel (m s^{-1} ; red) and terrain-normal (m s^{-1} ; blue) wind and computed Fr (magenta, black) using AJAX data from 2250 UTC 10 Mar to 0005 UTC 11 Mar 2016. The magenta and black lines represent the Fr computed using different mountain heights h (800 m and 1 km, respectively). The shaded circle (green) represents the Santa Cruz mountains (Mt. Santa Cruz) area. The magenta triangle represents the peak of Mt. Santa Cruz.

At 0900 UTC 11 March, the dominant flow is still southwesterly (Fig. 2b), but a southerly component has increased and the horizontal wind has become more meridionally oriented, as has the elongated band of high water vapor associated with the AR. The main axis of relatively cold air aloft has a small center situated well offshore the California coast associated with the high PV air in the midtroposphere (Figs. 2e,h). The region of maximum horizontal temperature gradient shifts farther south, and temperatures are slightly cooler inland north of the San Francisco Bay Area.

By 1800 UTC 11 March, higher water vapor has moved inland along with cooler temperatures, and the surface low and upper-level PV trough have weakened (Fig. 2i). Interestingly, the strong upper level trough shown on 10 March appears to undergo anticyclonic Rossby wave breaking (Fig. 2g). Ryoo et al. (2015) demonstrated that 66% of the AR events from 1997 to 2010 were associated

with anticyclonic Rossby wave breaking, and those AR events appear closely linked to this upper-level dynamical evolution. The large-scale upper-level troughs over northern California may also provide favorable conditions for the formation of TTAs during AR events.

b. Observed vertical profiles of AJAX measurements

Consistent with the MERRA-2 data shown in Fig. 2a, the predominant wind direction measured in situ was southwesterly at about 2300 UTC (Fig. 3b). However, there is a subtle shift in horizontal winds at the lowest level, particularly evident in the northern part of the transect (around 37° – 37.2°N , 122.4°W), with winds deflecting northward to more parallel to the coast (red circles in Figs. 3b,c). This turning of wind direction along the transect from the southeast (SE) to the northwest (NW) appears to be a signature of the emergence of the first TTA during this AR event and is

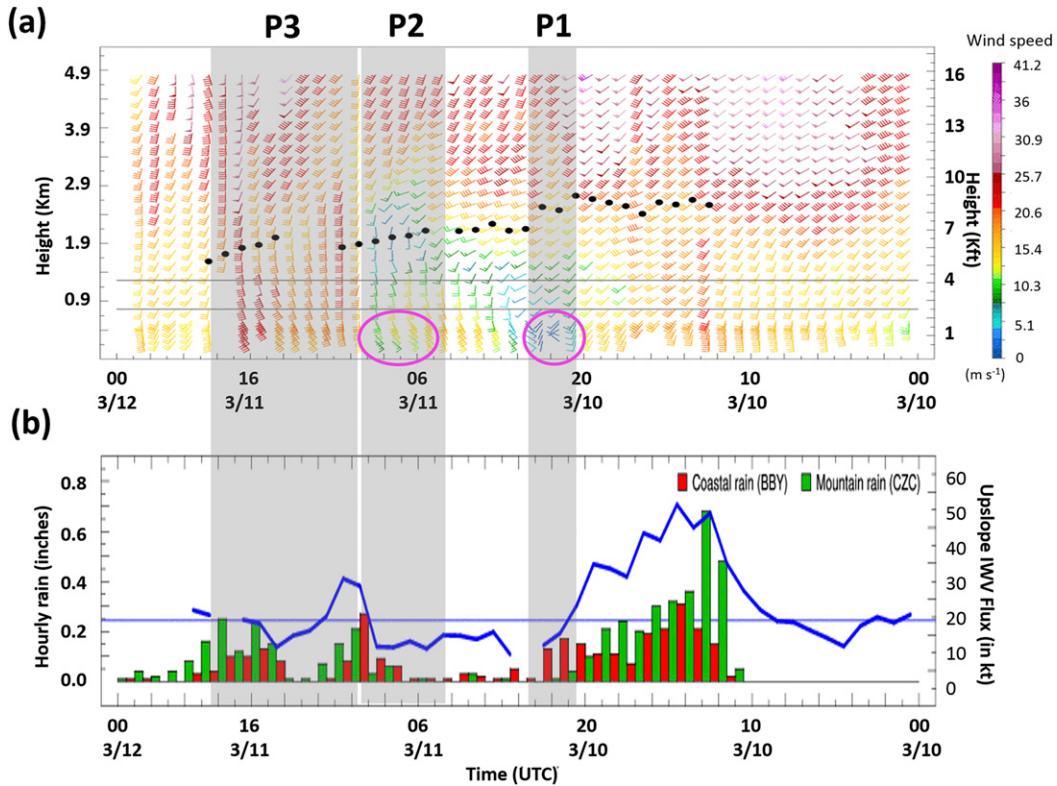


FIG. 4. Time series of (a) wind speed as a function of altitude at Bodega Bay (BBY; kt, where $1 \text{ kt} \approx 0.51 \text{ m s}^{-1}$) and (b) observed hourly precipitation (in.) over the BBY (coast, red) and the Cazadero (CZD, mountain, green) sites, with the upslope integrated water vapor flux (blue; kt) observed by the wind profiler at BBY from 0000 UTC 10 Mar to 0000 UTC 12 Mar 2016. Gray-shaded boxes in (a) and (b) identify the time periods for further discussion: P1 between 2100 and 2300 UTC 10 Mar, P2 during 0500–0900 UTC 11 Mar, and P3 during 1000–1800 UTC 11 Mar. The black dots in (a) represent the observed hourly profiler-derived snow level. The figure is initially obtained from <https://www.esrl.noaa.gov/psd/data/obs/datadisplay/>. Note that the time axis is from right to left to represent the eastward advection of the AR storm. The magenta circles during P1 and P2 refer to the occurrence of the first and the second TTA, respectively.

manifest also in the evolving water vapor flux. The time series of water vapor and winds measured by AJAX over all altitudes are shown in Fig. S1 in online supplemental material.

TTAs due to low-level blocking may occur during low Fr conditions, $\text{Fr} < 1$, with favorable synoptic conditions characterized by relatively weak large-scale cross-barrier flow and relatively high static stability (recall that $\text{Fr} = U/Nh$ with U the barrier-normal wind speed, h the barrier height, and N the Brunt–Väisälä frequency). In the most straightforward analysis, Fr is estimated using the dry Brunt–Väisälä frequency, $N_d^2 = (g/\theta)(d\theta/dz)$, where θ is potential temperature, and g is an acceleration of gravity. Many studies, however, have shown that moist Brunt–Väisälä frequency N_m (Durran and Klemp 1982; Hughes et al. 2009) is a more appropriate choice when air impinging on mountains is saturated. Since N_m is only applicable in saturated conditions, N_m is used here only when

the near-surface (<500-m altitude) relative humidity (RH) exceeds 90%; otherwise, N_d is used.

Figure 3d shows in situ wind speeds and Fr values. On March 10, the meridional wind is 5–10 m s⁻¹ higher than the zonal wind, especially around about 1 km above ground level (AGL) (not shown). Since the coastal mountains just inland approximately parallel the coastline, we estimate the terrain-parallel wind by the coast-parallel wind component. The horizontal wind components $\mathbf{U} = (u, v)$, the angle β (about 56.3°) between the coastline from the north direction, and the angle α [where $\alpha = \tan^{-1}(v/u) - \beta$] between the horizontal wind vector and the line normal to the coastline are used for computing the terrain-parallel component and terrain-normal component of the wind near Mt. Santa Cruz. AJAX measures the potential temperatures θ with respect to altitude, longitude, latitude, and time. At the given location where there is vertical transect, we calculated the vertical potential temperature gradient

TABLE 1. Characteristics of TTAs and precipitation over different periods (P1, P2, and P3) during 10–11 March 2016 AR events over BBY and Mt. Santa Cruz. The low-level wind defines wind below 800 m.

Period	Period 1 (P1)	Period 2 (P2)	Period 3 (P3)
Start	2100 UTC 10 Mar 2016	0500 UTC 11 Mar 2016	1000 UTC 11 Mar 2016
End	2300 UTC 10 Mar 2016	0900 UTC 11 Mar 2016	1800 UTC 11 Mar 2016
Low-level ($<\sim 800$ m) wind direction	Onshore-directed deflected wind pattern toward the coast, southeasterly	Offshore-directed wind, southeasterly	Southeasterly and southwesterly
Low-level ($<\sim 800$ m) wind speed	$<5 \text{ m s}^{-1}$	$<15 \text{ m s}^{-1}$	$>15 \text{ m s}^{-1}$
Precipitation ratio [mountain/coast (i.e., CZD/BBY)]	<1.5 on average	<1.5 on average	>2.5 on average
Low-level blocking (coastal barrier jet formed)	Yes	No	No
Gap flows	No	Yes	Merged with pre-cold-frontal LLJs
TTA formed	Yes (CBJs)	Yes (gap flows)	Gap flows merged with pre-cold-frontal LLJs
Vertical motion	Mild ascent offshore	Moderate ascent offshore	Strong ascent over the coastal mountain
Observational data Source	AJAX aircraft data near Mt. Santa Cruz and wind profiler data over BBY, tipping-bucket rain measurement	Wind profiler data over BBY, tipping-bucket rain measurement	Wind profiler data over BBY, tipping-bucket rain measurement
Notes	Low-level blocking (CBJ) due to the coastal terrains	Gap flows due to pressure and temperature difference between the Petaluma gap entrance and exit	Gap flows merge with pre-cold-frontal LLJs

by calculating $\partial\theta/\partial z$. The terrain-parallel wind increases at the lowest altitude and between 0.4 and 0.9 km AGL (red profile in Fig. 3d). As mentioned earlier, we observed the initial development of the wind deflection to be parallel to the coast, identifying the formation of the initial coastal barrier jet (CBJ; the first TTA) from AJAX data. The increasing terrain-parallel wind occurs during a period when $\text{Fr} < 1$, consistent with this CBJ being due primarily to low-level terrain blocking related to the relatively weak onshore flow and high static stability at lower levels during this period.

The topographic effect of terrain blocking on the wind field occurs within a Rossby radius of deformation of the topography L (Gill 1982; Luna-Niño and Cavazos 2018), where $L = (Nh)/f$, with f being the Coriolis parameter (Valenzuela and Kingsmill 2018). When low-level terrain blocking exists (i.e., $\text{Fr} < 1$), L is an order of ~ 100 km or less for a terrain height in the coastal region (≤ 1 km), N of 0.01 s^{-1} , and f about 10^{-4} s^{-1}). For computing Fr, we used the observed terrain-normal wind as U . The transect AJAX flew was ≤ 15 km off the California coast (except when crossing the mouth of Monterey Bay), so the measured winds were generally affected by topography, and well within L . Although ideally, upstream cross-barrier observed winds should be used for U to compute Fr, the mean velocity of the upstream flow appeared to be slightly less than or the same as near

the coast around 2000–2300 UTC 10 March, especially during the period when terrain blocking occurs (supported by the model simulation, not shown). Therefore, uncertainties in choice of the upstream winds for estimating Fr are unlikely to affect this interpretation.

c. Observed TTAs from NOAA wind profilers and precipitation measurements

Augmenting observations of the first TTA from AJAX flight measurements, which suggest a terrain blocking mechanism, we further examined the characteristics of TTAs during this AR event using wind profilers and hourly rain rates at BBY during the period 10–11 March 2016 (Fig. 4). Around 2300 UTC 10 March, the wind below 0.5 km starts changing its direction toward southeasterly, approximately parallel to the coastal terrain. The southeasterly signature persists between 2300 UTC on 10 March and roughly 1800 UTC on 11 March, developing from lower altitudes of ~ 0.4 km up to 1.4 km above the surface.

To better identify distinct mechanisms related to TTAs occurring during the AR, we divide the AR into three subperiods based on wind fields, with key differences summarized in Table 1. Period 1 (P1) is identified when the low-level wind ($<\sim 800$ m) is southeasterly with speed less than 5 m s^{-1} , occurring

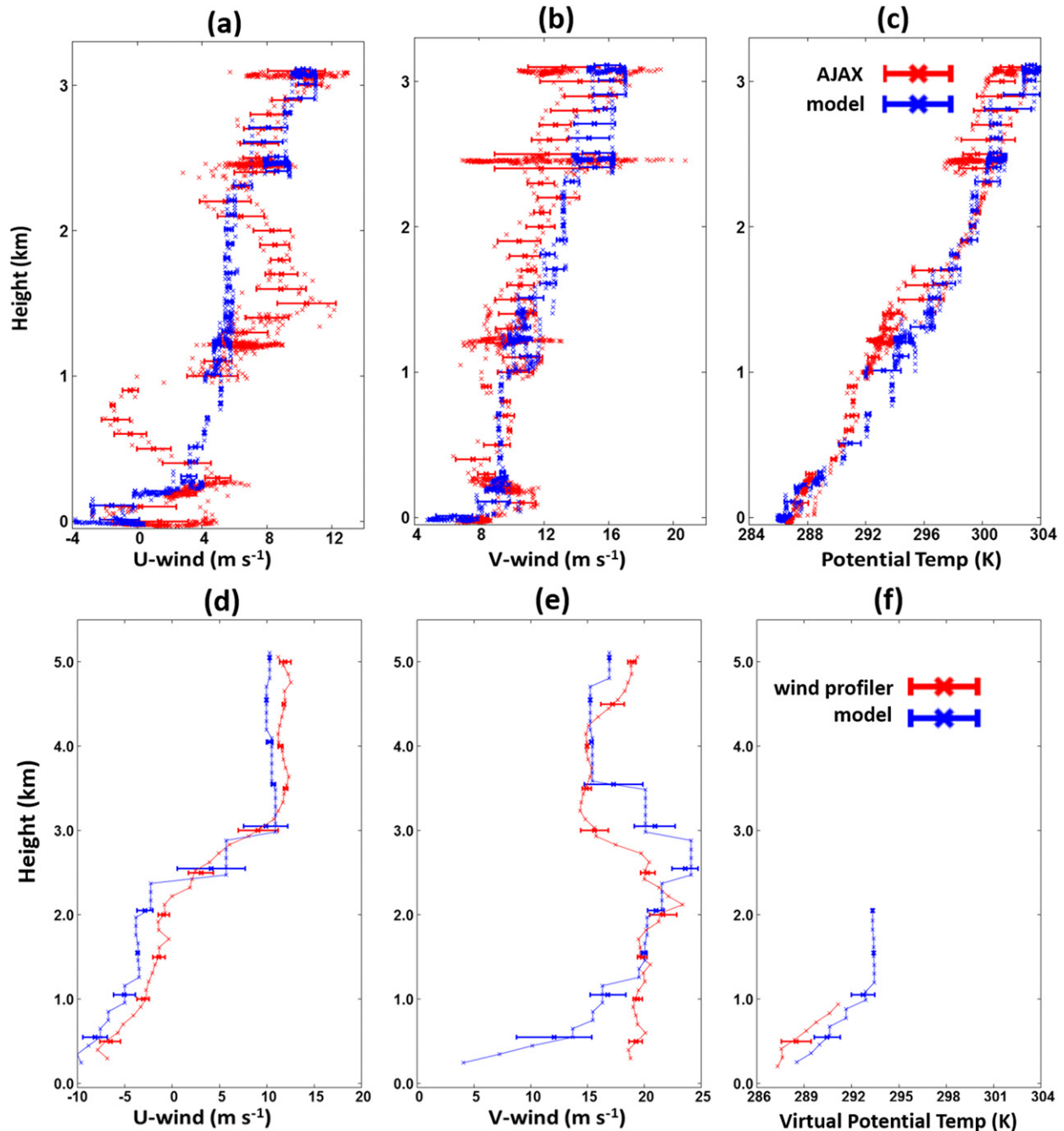


FIG. 5. Vertical profiles of (a) zonal wind (m s^{-1} ; U -wind), (b) meridional wind (m s^{-1} ; V -wind), and (c) virtual potential temperature (K) (a)–(c) measured by the AJAX flight (red) and modeled by the WRF Model (blue) interpolated along the AJAX flight track from 2250 UTC 10 Mar 2016 to 0005 UTC 11 Mar 2016. (d)–(f) As in (a)–(c), but measured by the BBY wind profiler (red) and modeled by the WRF Model (blue) along the wind profiler at 1100 UTC 11 Mar 2016. One standard deviation from the mean value at each altitude is presented with the horizontal bar.

during 2100–2300 UTC 10 March 2016. During this period, there is also a deflected wind toward the coast in the 10-m modeled wind field nearest the aircraft transect (see Fig. 7a). Period 2 (P2, 0500–0900 UTC 11 March) is defined when the low-level wind (<~800 m)

is southeasterly with speed < 15 m s^{-1} , and strong on-shore (westerly and southwesterly) flow occurs above 1 km. Period 3 (P3) is defined when the low-level wind (<~800 m) is still southeasterly but with wind speed > 15 m s^{-1} , which captures the time between 1000 and

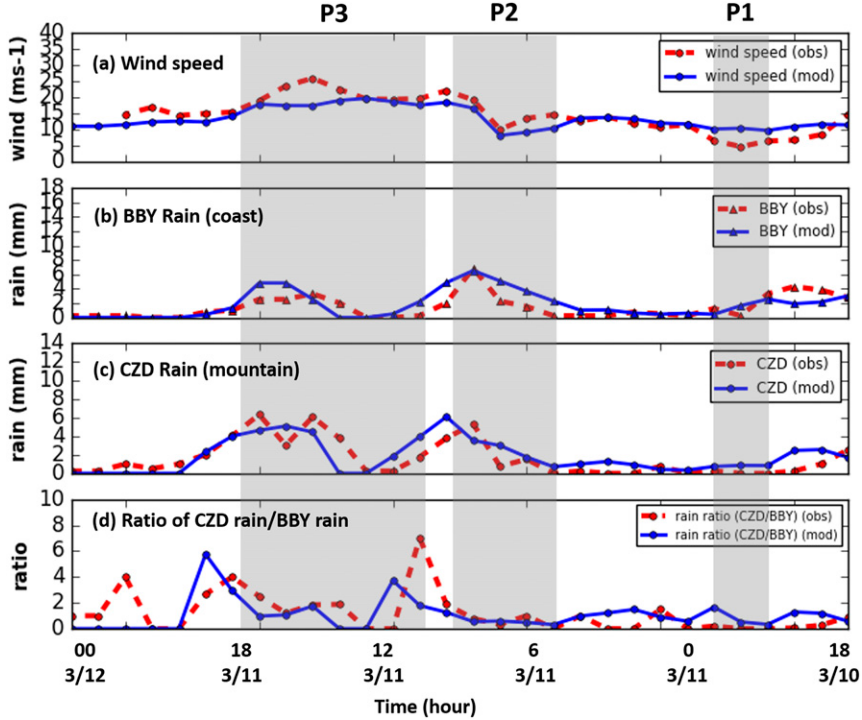


FIG. 6. Time series of (red) observed and (blue) modeled (a) wind speed at BBY, (b) precipitation over BBY (coastal region), (c) precipitation over CZD (mountain region), and (d) rain ratio (CZD/BBY) from 1800 UTC 10 Mar to 0000 UTC 12 Mar 2016. Observed wind data is only available over BBY from the wind profiler.

1800 UTC 11 March 2016. The strongest low-level winds occur during P3 at \sim 1.2 km above the surface at 1500–1600 UTC 11 March, related to the pre-cold-frontal LLJ (see Fig. 4a).

All these wind features are associated with locations of enhanced precipitation during the different periods. Mountain precipitation (green bars in Fig. 4b) is abundant during 1000–2100 UTC, but begins to diminish around the time when the weak southeasterlies emerge (2300 UTC 10 March, P1) and does not return until 0900 UTC 11 March as P2 ends. The upslope IWV fluxes (blue line) weaken during the early period of southeasterlies (2300 UTC 10 March) but strengthen again around 0900 UTC and 1500 UTC 11 March. The up-slope wind speeds and IWV fluxes closely correspond (not shown). During P1, the coastal precipitation increases (red bars), in contrast with the mountain precipitation. Coastal precipitation also increases during the end of P2. During P3, mountain precipitation increases as upslope IWV flux (and wind speed) increases. Finally, after 1800 UTC 11 March, the wind direction turns to southwesterly, and the upslope IWV flux significantly decreases, leading to an overall reduction of precipitation. The winds and IWV flux patterns in Fig. 4 are consistent with the observed

precipitation features over the BBY (coastal area) and the CZD (mountain area) sites.

d. Model–observation comparison

The upper panels in Fig. 5 show vertical profiles of zonal wind, meridional wind, and potential temperature measured by 1) AJAX and the WRF model simulation interpolated along the flight track for 2200–2400 UTC 10 March 2016, and 2) the wind profiler and WRF Model simulation interpolated along the wind profiler at 1100 UTC 11 March 2016. Most features of the model simulation are within the range of observed winds and potential temperatures. There are, nevertheless, some notable differences. The model tends to underestimate the observed meridional wind below 1.5 km while it overestimates the observed winds above 2 km. Discrepancies are found between the observations and WRF simulation in zonal wind shear between 500 m and 2 km (see Fig. 5a). Possible contributors to the differences are 1) inadequacies in simulating vertical shear related to the TTA from low-level terrain blocking. Notably, the wind profiler at 2300 UTC over BBY also indicated some disagreement with WRF winds below 2 km (not shown). 2) Possible underestimation in the WRF Model of the shear layers and shear-generated turbulence of

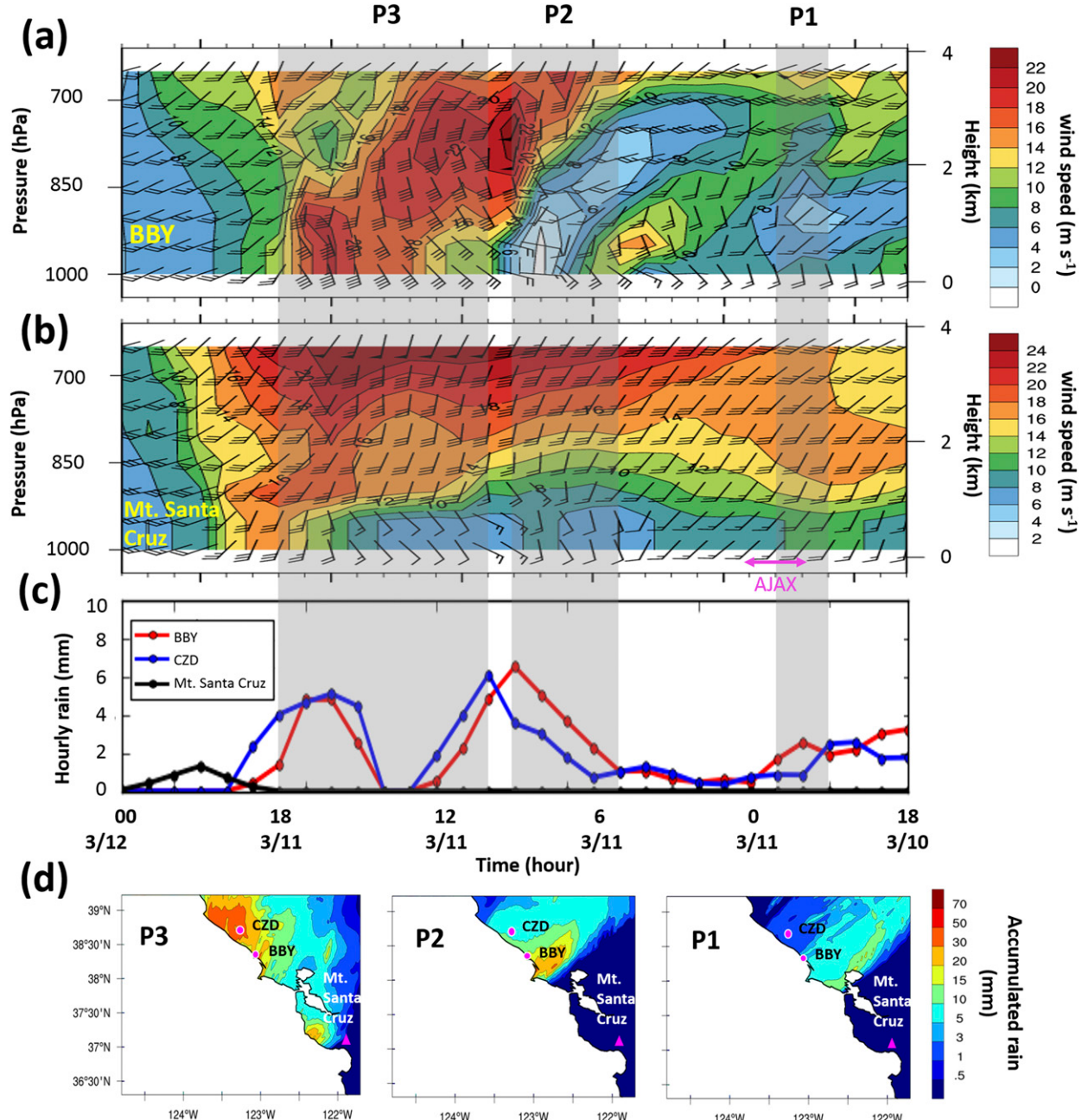


FIG. 7. Time–height cross section of modeled meridional wind speed (m s^{-1}) overlaid by the total horizontal wind at (a) BBY and (b) Mt. Santa Cruz from the WRF Model simulation. (c), (d) The modeled precipitation (mm) (c) at coastal (BBY) and mountain (CZD and Mt. Santa Cruz) sites and (d) averaged over the periods P1, P2, and P3. The time axis in (a)–(c) is from right to left to represent the eastward advection of the AR storm.

the low-level blocked flow at these levels (Houze and Medina 2005), so that the model fails to adequately capture the presence of the CBJ around 800 m and above it (1.5 km) over Mt. Santa Cruz at the time of measurement. A similar discrepancy was found between the model and BBY wind profiler data comparison at the same time (~ 2300 UTC 10 March 2016).

3) Model potential temperatures also tend to be warmer than observations except below 0.5 km, indicating low-level static stability is higher in the model than observations, which may contribute to simulation and prediction errors. Due to the different temporal and spatial resolution and data availability, a direct comparison between the WRF Model and AJAX data

is also challenging to make. While these model–observation discrepancies are notable and merit additional study, the overall ability of the model simulation to replicate most observed wind and potential temperature features supports our interpretation for many important processes during this event.

Figure 6 shows the comparison of average wind speed (up to 5 km from the surface) and 1-hourly rain rate, from both observation (red) and WRF Model simulation (blue). The model wind overestimates observed values by $2\text{--}4 \text{ m s}^{-1}$ around 1900 UTC 10 March and 0100 UTC 11 March, but otherwise, has similar features and magnitudes. In general, model precipitation over BBY overestimates observed precipitation, although the overall pattern can replicate the observed pattern for some periods. Model precipitation over CZD generally lags behind observed precipitation during P2 and P3, and it may underestimate precipitation totals. The ratio of mountain (CZD) to coastal (BBY) rain (**Fig. 6d**) has higher values (>2.5 on average) starting from ~ 1000 UTC 11 March to the 1800 UTC 11 March, corresponding to P3. Slightly lower values (<1.5 on average) over P1 and P2 are found. This is consistent with the results of Valenzuela and Kingsmill (2017), who reported coastal precipitation (i.e., at BBY) tends to increase when TTAs are developing. We also compared the maps of 6-hourly accumulated NCEP Stage IV precipitation (Nelson et al. 2016; <http://www.emc.ncep.noaa.gov/mmb/ylin/pcpnl/stage4/>) and WRF simulated precipitation during the 10–11 March 2016 AR case in Fig. S2. In general, NCEP Stage IV and modeled precipitation show similar features regarding variability, except for the Sierra Nevada mountain region and the coastal range, where both measuring and predicting precipitation over mountainous regions pose particular challenges (Strangeways 1996; Smalley et al. 2014).

4. Characteristics of TTAs simulated from WRF-ARW

a. Kinematic characteristic of TTAs

To further understand the detailed kinematic structure and characteristics of TTAs in conjunction with the pre-cold-frontal LLJs, we examined time series of modeled meridional wind and precipitation at both BBY, CZD, and Mt. Santa Cruz in **Fig. 7**. The closest distance from the AJAX flight track to Mt. Santa Cruz (peak elevation ~ 1154 m) was ~ 40 km, and a second peak (elevation ~ 740 m) was also located ~ 15 km from the flight track. Over Mt. Santa Cruz (**Fig. 7b**), the modeled wind does not indicate southeasterly flow until around 0500 UTC 11 March, in

comparison to the in situ observation of southeasterly wind emerging around 2300 UTC 10 March (see red circle in **Fig. 4**). This is consistent with the results shown in **Fig. 5a**, highlighting the difficulty in modeling low-level zonal wind shear between 500 m and 2 km in this event.

Figure 7a shows a distinctive vertical gradient of meridional wind speed at BBY at this time, centered ~ 1 km aloft, with values of $\sim 5 \text{ m s}^{-1}$ below and 25 m s^{-1} above. At BBY, different wind patterns (wind direction and wind speed) were observed over two periods: 2100–2300 UTC 10 March (identified as P1), and 0500–0900 UTC 11 March (identified as P2). Consistent with **Fig. 4**, around 2300 UTC 10 March (during P1), the surface winds were mainly southeasterly, and a pre-cold-frontal LLJ structure was absent. The zonal wind (easterly) patterns showed that the airflow was directed approximately parallel to the coastal mountains from SE to NW, consistent with a CBJ (**Fig. 7a**). Around 0500 UTC 11 March (during P2), a meridional pattern similar to that around 2300 UTC 10 March was also found with a strong jet structure and relatively dry air (low specific humidity q , not shown). The potential temperature decreases with time toward the end of P3, indicating a cold front passage after the AR event (not shown). Both observational and model data show more coastal precipitation (BBY) than mountain precipitation (CZD and Mt. Santa Cruz) during P1 and P2 (**Figs. 4, 6, and 7**). Conversely, mountain precipitation is slightly more abundant during P3 (CZD) and after (Mt. Santa Cruz, **Figs. 7c,d**). This is consistent with the finding of Valenzuela and Kingsmill (2017), who showed that the mountain-to-coast rainfall ratio was lower (~ 1.4) when there was terrain trapped flow (TTA), while the ratio increased (~ 3.2) without TTA.

To further understand the processes of TTA formation, we examined the WRF Model flow patterns, temperatures, and wind speeds during two different periods. **Figures 8a–c** shows the WRF-simulated surface temperature overlaid by 10-m wind vectors; **Figs. 8d–f** show 10-m wind speed (colors) and sea level pressure (isobars). At 2300 UTC 10 March (**Figs. 8a,d**, corresponding to P1), relatively warm and mild onshore-directed southwesterly flow is evident that changes direction to parallel the coast, forming a weak CBJ (the first TTA). At this time, the precipitation over the coastal region north of San Francisco Bay increases slightly (**Figs. 7c,d** and 8g). Consistent with the Fr analysis using aircraft data shown in **Fig. 3**, Fr values computed from model data are <1 at the north of San Francisco Bay Area including BBY and Mt. Santa Cruz around 500 m at 2300 UTC 10 March, supporting

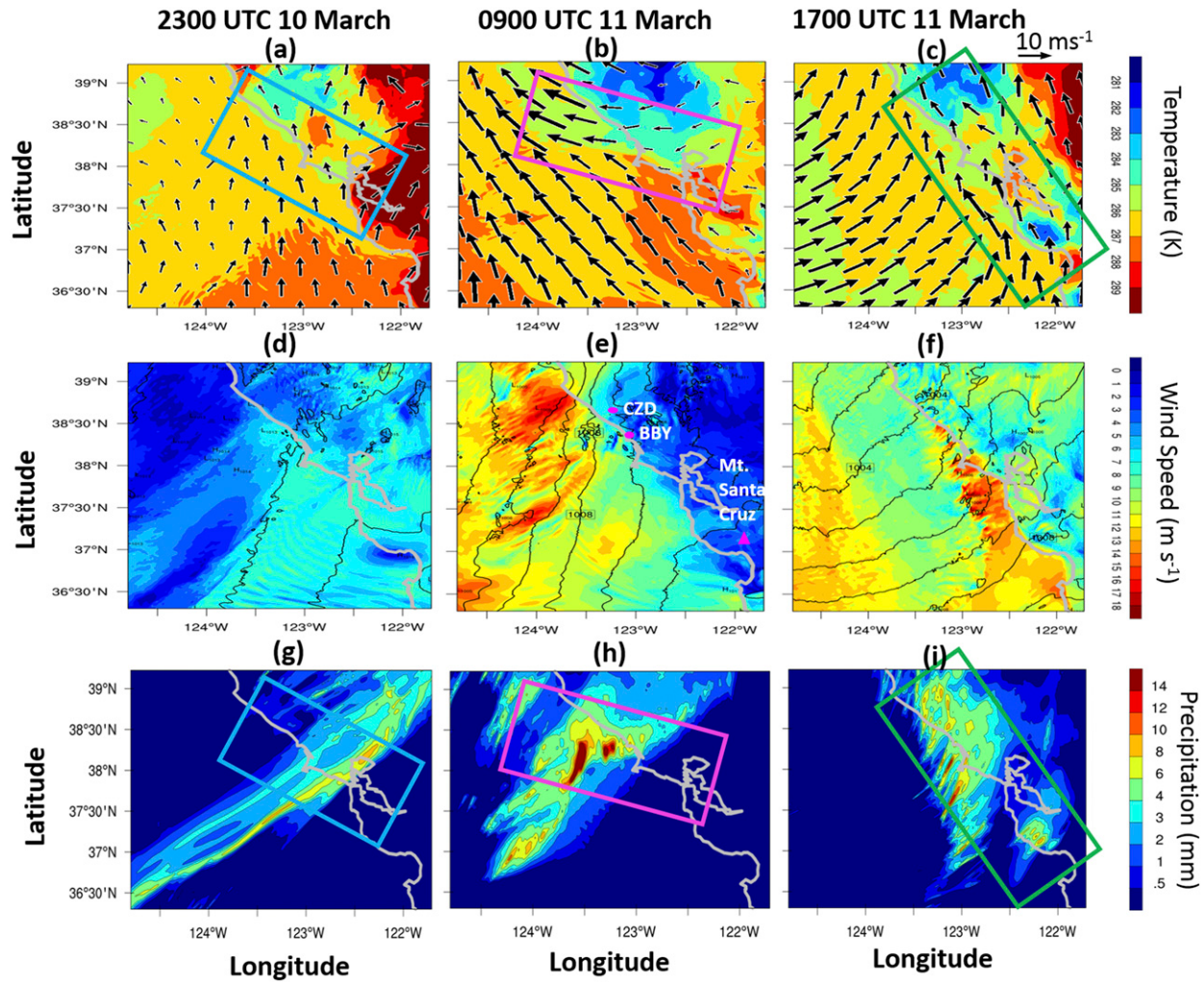


FIG. 8. WRF-simulated (a)–(c) surface air temperature (K; shaded) overlaid by 10-m wind vectors (arrows), (d)–(f) 10-m wind speed (m s^{-1} ; shaded) overlaid by sea level pressure (hPa; black line) and (g)–(i) model precipitation (mm) at (left) 2300 UTC 10 Mar, (center) 0900 UTC 11 Mar, and (right) 1700 UTC 11 Mar 2016. Each box represents the onshore-directed deflected flows in (a), offshore-directed gap flows in (b), and pre-cold-frontal LLJs merging with offshore flows in (c).

the earlier interpretation of terrain flow blocking for this TTA event.

From 0500 UTC 11 March to 0900 UTC 11 March (corresponding to P2), more organized southeasterly flow develops parallel to the coastline (Fig. 8b). Offshore-directed gap flow from the Central Valley turns anticyclonically near the coast, further contributing to a strong TTA (the second TTA). Relatively cold air exited from the interior through the Petaluma gap and crossed over BBY, augmenting the gap flow due to pressure gradients associated with approaching synoptic-scale AR storm (Figs. 8b,e). Note that the maximum speed of the offshore-directed gap flow tends to be 2–3 times larger than that of the ambient synoptic flow (see Fig. 8b). This implies that the gap flow can determine the size of TTA, consistent with

Olson et al. (2007), which a gap flow can extend the size of BJ by changing its structure and intensity over the southeast Alaskan coast. Precipitation increases over the area where the temperature gradient is large and tends to increase over the coastal region (Fig. 8h).

At 1700 UTC 11 March (Figs. 8c,f, corresponding to P3), confluence of the synoptic flow offshore with gap winds is located near the coast, especially south of Mt. Santa Cruz and Monterey Bay, leading to strong wind speeds combined with high water vapor transport (not shown). This combination can lead to high precipitation rates over favored mountain regions, as shown in Fig. 8i. Over the three periods throughout this AR event, different wind directions and speeds associated with the TTAs were closely related to

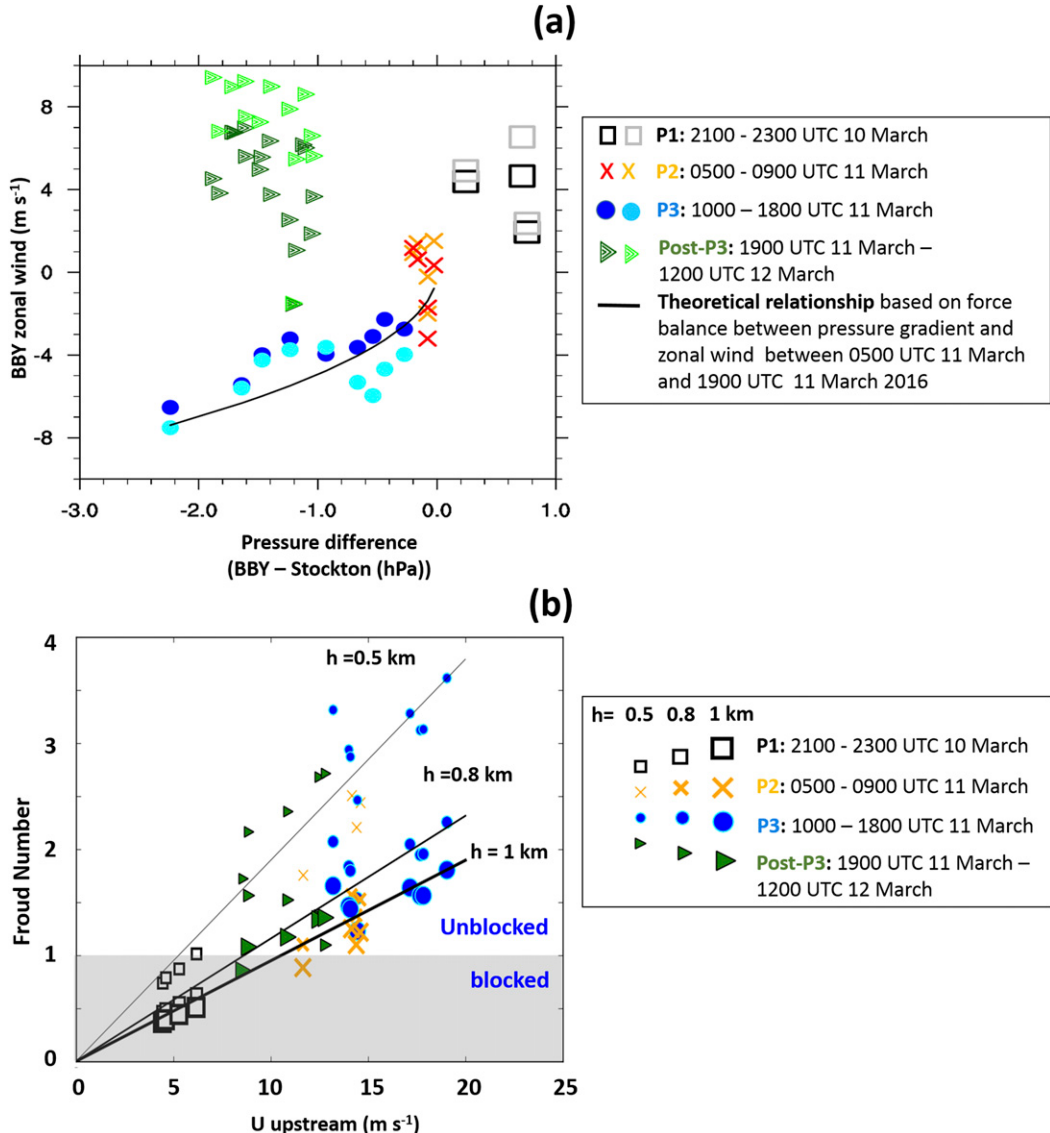


FIG. 9. (a) A scatterplot of the WRF-simulated hourly surface pressure difference between BBY and Stockton, CA, vs hourly surface zonal winds (black, red, blue, dark green) and approximately below 500 m layer-averaged zonal wind (gray, orange, cyan, green) at BBY. The black line in (a) stands for the theoretical relationship between pressure gradient, surface friction, and gap flows provided by Mass et al. (1995) and Valenzuela and Kingsmill (2015). (b) Fr analysis using modeled upstream U (m s^{-1}) and N_m (s^{-1}) for different mountain heights ($h = 0.5, 0.8, 1 \text{ km}$). Each regression was computed for U and Fr using different h . The different colors correspond to a different period for P1 (black), P2 (orange), P3 (blue), and post-P3 (green). The different sizes correspond to different mountain heights from 0.5 to 1 km (from smallest to largest). The gray box area is indicated as blocked when Fr is less than 1.

precipitation patterns and intensities over the coastal and mountain regions.

b. Forcing mechanisms of TTAs: Low-level blocking and gap flow

To confirm that the TTA occurring during P2 is produced by the Petaluma gap flow, we examined the relationship between the pressure gradient and wind at

BBY to determine if this event followed the theoretical relationship shown by Valenzuela and Kingsmill (2015, 2018). The hourly pressure difference was calculated between BBY and Stockton, located at the eastern end of the Petaluma gap. Zonal winds were derived using the simulated 0–500-m layer-mean winds and 10-m wind. Figure 9a shows the hourly model data, with different symbols representing P1, P2, P3, and post-P3

periods. The solid line shows the theoretical relationship used to derive the gap flow as a function of the pressure gradient (Mass et al. 1995). We include the frictional effects using the same drag coefficient used in Mass et al. (1995). The boundary layer depth (PBLH) is estimated as 700 m, and the average air density of 1.24 kg m^{-3} was chosen based on the observations at BBY and Stockton, used in Valenzuela and Kingsmill (2017). Sensitivity of the result to different PBLH (500, 700, and 1000 m) was small (not shown).

We focus first on the period from 0500 to 1800 UTC 11 March during P2, when the second TTA forms, and P3, when the TTA merges with the pre-cold-frontal LLJ. Figure 9a shows that the model data agrees with the theoretical force balance relationship between the pressure difference and the zonal wind due to gap flow. In contrast, the conditions before 0500 UTC (P1, open squares) and after 1900 UTC 11 March (post-P3, filled triangles) significantly depart from the relationship, indicating that these periods are not associated with gap flow.

Figure 9b shows Fr calculated using WRF-simulated wind during different analysis periods and its sensitivity to the terrain height. The upstream wind U is less than $\sim 8 \text{ m s}^{-1}$, and N is $\sim 0.01 \text{ s}^{-1}$ over the area averaging both BBY and CZD during P1 (open squares). The Fr shows that the flow has low U/Nh (i.e., $\text{Fr} < 1$) when the mountain height h is set to 0.5, 0.8, or 1 km. This indicates that blocked CBJs are well represented in the WRF simulation along the windward side of the California coastal range at that time. However, during P2 (red and orange \times symbols) and afterward, combining the strong upstream winds and N_m produces a larger Fr, up to about 4 (e.g., $U = 20 \text{ m s}^{-1}$, $N \sim 0.01 \text{ s}^{-1}$, $h = 0.5 \text{ km}$). Thus the P2 TTA is not caused by terrain blocking. Comparable stabilities (N_m , ranging from 0.009 to 0.015) exist throughout P1–P3, but distinct flow patterns associated with different mechanisms occurred across the periods. The TTAs formed during P1 and P2 were likely produced by different processes, mainly related to a different source of the airmass.

Nearly all time during P1 had $\text{Fr} < 1$, regardless of the height of the terrain h , supporting an interpretation of a terrain blocked flow. However, most times during P2 and P3 had $\text{Fr} > 1$, with blocking only possible when h is large. Valenzuela and Kingsmill (2018) showed that in their study TTA terrain blocking was likely associated with high inland orography. Here, however, it appears that low-level blocking can also be generated by relatively low coastal orography ($h \sim 500\text{-m}$ elevation), although it is relatively weaker and more short lived than terrain blocking in the Valenzuela and Kingsmill study.

Following P1, but before the second TTA develops in P2, both coastal and mountain precipitation decreases significantly (Figs. 4b, 6) due to a reduction of moisture and temperature inland (not shown). This can be seen in Figs. 2h and 2i when there is a deep penetration of dry, cold air down to the midtroposphere ($\sim 500 \text{ hPa}$), associated with the large-scale upper-level trough. In addition to changes in precipitation amount, Hughes et al. (2009) found that the ratio of precipitation at mountain (steepest slopes $\sim 80 \text{ m km}^{-1}$) and coastal (gentlest slopes $\sim 10 \text{ m km}^{-1}$) sites was close to 1:1 for low Fr but increased to nearly 4:1 for high Fr. This is consistent with our result of more coastal precipitation during P1 with low Fr, P2 with high Fr, and relatively more mountain precipitation during P3 with high Fr (Fig. 6d). Relationships suggested in Fig. 9 could be strengthened in the future if additional offshore wind profile, temperature, and water vapor observations could be obtained to better estimate detailed fields of N_m and Fr.

c. Mixing diagnostic

The diagnostic Q is used to identify periods when stretching of airmasses increases interfacial area and thus facilitates mixing across boundaries. Figure 10a shows the time series of the Q calculated over BBY, CZD, and Mt. Santa Cruz [vertically averaged up to 700 hPa ($\sim 3 \text{ km}$)] during the study. The bottom panels are longitude–pressure cross sections of Q (averaged over $36.5^\circ\text{--}40^\circ\text{N}$) at the three periods indicated by vertical bars in Fig. 10a. Also shown are water vapor mixing ratio overlaid by the zonal and vertical wind vector, interacting with the complex coastal mountains (see the upper panels of Figs. 10b–d).

The time series of Q shows that regional differences in mixing between BBY and CZD are small, with slightly less mixing expected in the Mt. Santa Cruz area during P2 and P3. All three locations show increasing mixing (more positive and high values of Q) near the end of P2, with maxima in mid (BBY and CDZ) to late (Mt. Santa Cruz) P3 as the pre-cold-frontal LLJ intensifies. During P1, enhanced water vapor (q) is seen offshore and on the windward side of the mountain ($124^\circ\text{--}122.8^\circ\text{W}$) at 2300 UTC 10 March 2016. But Q is low both offshore and onshore, indicating mixing is weak during the low-level blocking period (Fig. 10b).

In contrast, during P2, easterly flow from inland, related to the gap flow from the mountain range, occurs at lower levels around 950 hPa ($\sim 540 \text{ m}$) by 1100 UTC. Strong ascending flow associated with the pre-cold-frontal LLJ (wind speed $> 20 \text{ m s}^{-1}$) occurs offshore during P2 and intensifies as the easterly, offshore-directed flow emerges in P3. The positive vertical

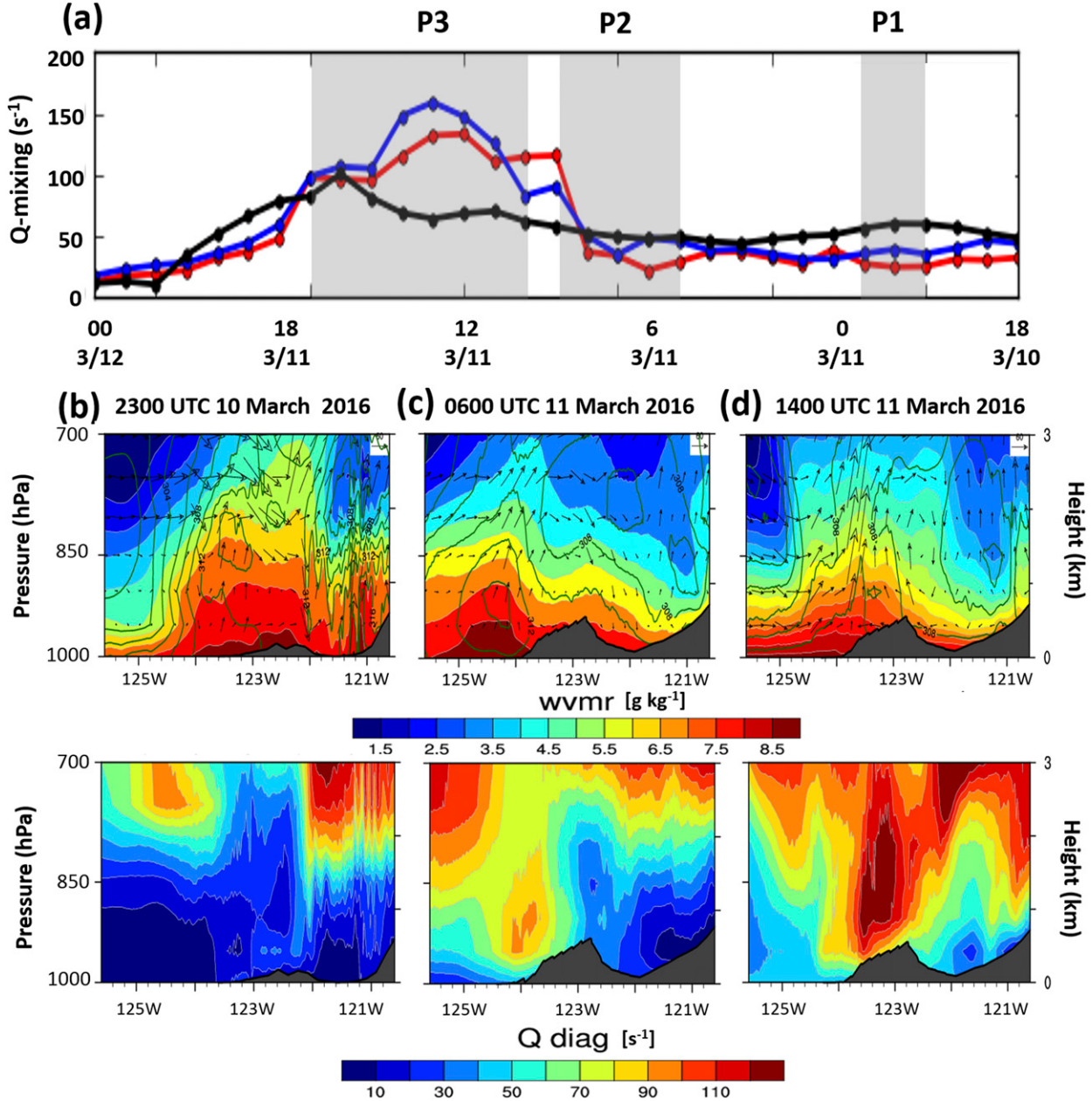


FIG. 10. (a) Time series of Q diagnostic (s^{-1}) averaged over BBY (red), CZD (blue), and Mt. Santa Cruz (black) from 1800 UTC 10 Mar to 0000 UTC 12 Mar. (b)–(d) Longitude-pressure cross section of simulated (top) water vapor mixing ratio ($g\ kg^{-1}$) and zonal u and vertical wind w vectors ($m\ s^{-1}$; w is multiplied by scale factor of 100) and (bottom) Q diagnostic (s^{-1}) averaged over 36° – 38.5° N at 2300 UTC 10 Mar and averaged over 36.5° – 40° N at 0600 UTC 11 Mar and 1400 UTC 11 Mar 2016, respectively.

motion was stronger offshore ($>124^{\circ}$ W) than the windward side (124° – 122.8° W), while the negative vertical motion emerged over the lee side of the mountain ($\sim 122^{\circ}$ W) during P2. As the ascent and upslope IWV increases at the end of P2, precipitation was enhanced at the end of P2 (see Fig. 4b). During P3, the mixing facilitates the lifting of the pre-cold-frontal LLJs when the offshore-directed gap flow

merges with the pre-cold-frontal LLJs, which may enhance mountain precipitation and inland moisture transport (see Figs. 7d, 8i, Fig. S3).

The vertical motions during P2 and P3 shown in the upper panels of Figs. 10b–d are consistent with the finding by Valenzuela and Kingsmill (2018), indicating that strong ascent occurs offshore over the TTA during TTA conditions while the ascent is slightly stronger

over the coastal mountain during non-TTA periods. The model-simulated vertical motions in P1 in our study show that weak ascent occurs offshore, especially when averaging over the small area where the terrain-blocking flow is observed (the upper panel of Fig. 10b). The mixing was mild in P1, increasing in P2, and stronger over the coast and coastal mountain in P3 (the lower panels in Figs. 10b–d). Overall, Fig. 10 quantitatively confirms that mixing between two air masses occurs during the end of P2 and P3, and it indeed affects the lifting of the pre-cold-frontal LLJs toward the windward side of the coastal mountain, controlling the precipitation distribution by favoring mountain precipitation when the pre-cold-frontal LLJs are lifted over the mountain, especially during P3.

5. Summary and conclusions

We have characterized the evolving relationships between terrain trapped airflows (TTAs), synoptic-scale meteorological conditions, and precipitation in northern California during the atmospheric river (AR) event of 10–11 March 2016 using aircraft measurements, surface observations, wind profiler data, and a 1-km resolution regional WRF simulation. We hypothesized that significant near coastal wind variations are related to different mechanisms for TTA formation, and that these wind variations have distinct impacts on precipitation locations and intensities during the evolution of an AR event. Two processes leading to TTA formation were identified: 1) low-level terrain blocking (i.e., CBJ) and 2) offshore-directed gap flow augmenting more coast-parallel synoptic-scale flow.

The two mechanisms led to TTAs at different times during this event. The low-level blocking mechanism was identified when horizontal wind direction backed from synoptic-scale westerly flow well offshore to more southerly flow close to the coast in a regime with a Froude number (Fr) < 1. The gap flow mechanism was identified when the relationship between the offshore-directed near-surface wind and the pressure difference between entrance and exit of the Petaluma gap followed the gap flow force balance in a regime with $Fr > 1$. During both of these TTAs, strong low pressure was centered offshore in association with a deep upper-level trough approaching the coast, with dry and relatively colder air inland.

The first type of TTA (a CBJ) occurred at the early stages of the AR event [period 1 (P1)] and it was associated with a maritime source of the air, relatively weak onshore flow, and a statically stable low-level environment. Shallow terrain blocking led to the TTA, although the magnitude of the coastal-parallel flow enhancement

was weak, with surface wind speed less than 5 m s^{-1} . During this period, both surface measurements and model simulations showed relatively more coastal than mountain precipitation. Valenzuela and Kingsmill (2018) found that in their study terrain blocking was likely connected to higher inland terrain. Our results show that terrain blocking can also result from the effects of the lower coastal orography ($h \sim 500\text{-m}$ altitude). This result suggests that weak, transient CBJs may also be formed by shallow coastal mountain blocking in sufficiently weak onshore flows and high low-level static stability, whereas larger scale and more intense terrain blocking with stronger onshore flows as in Valenzuela and Kingsmill may be connected to higher orography of the Sierras.

The second type of TTA formed in a fundamentally different regime than during P1. In period 2 (P2), winds strengthened with a component directed offshore. Our analysis showed that the formation of this TTA was due to offshore-directed gap-exit flow caused by the pressure and the temperature differences between the inland gap entrance and the coastal gap exit. The TTA during P2 exhibited surface wind speeds up to $\sim 15 \text{ m s}^{-1}$. Both TTAs extended offshore under 100 km, less than the Rossby radius of deformation (Loescher et al. 2006; Luna-Niño and Cavazos 2018). The maximum speed of the TTA in P2 was roughly 2–3 times larger than that of the ambient synoptic flow. As P2 progressed, the confluence of the TTA with an approaching pre-cold-frontal low-level jet (LLJ) led to the third AR period [period 3 (P3)]. P3 was characterized by more intense mountain precipitation and stronger wind speeds ($> 15 \text{ m s}^{-1}$) over the ocean and inland. Table 1 summarizes primary meteorological differences over the three periods.

Varying kinematic and thermodynamic characteristics between P1, P2, and P3 were closely associated with physical mechanisms for TTA formation, as well as interactions with the pre-cold-frontal LLJ, which led to widely varying precipitation spatial distributions and intensities. The first TTA was associated with coastal terrain blocking and favored coastal rather than mountain precipitation, consistent with earlier findings. The Q diagnostic indicated that dynamical mixing likely elevated the pre-cold-frontal LLJs, shifting high water vapor initially offshore and over the coastal regions onshore toward higher elevations inland, providing evidence for another mechanism influencing precipitation beyond what could be identified from previous single-point observations.

This study also showed that cold and dry air accompanied by a large-scale upper-level potential vorticity (PV) trough over northern California could facilitate the formation and development of TTAs, but more research is required to clarify to what extent such upper-level

features affect the formation of low-level TTAs. Other variables or conditions influencing TTA development, characteristics, and impacts also merit further investigation, including the residence time of low-level water vapor flux, change in the atmospheric stability, and low-level shear-generated turbulence to alter orographic precipitation during the evolution of AR events.

Our study is unique in describing TTA formation from two distinct forcing mechanisms during different stages in the evolution of a single AR event. The results indicate that TTAs can substantially affect the timing, locations, and intensity of precipitation in California during such events. Similar effects appear likely to occur as well elsewhere along the U.S. West Coast. Further work to better observe, understand, and model TTAs will help build the scientific basis for improving forecasts and early warnings of high-impact weather from AR events that so commonly affect the U.S. West Coast as well as many other coastal regions around the world with complex terrain.

Acknowledgments. The authors gratefully appreciate the support and partnership of H211 L.L.C, with particular thanks to the pilots, R. Simone and T. Grundherr, who flew expertly in bad weather to get AJAX data. We give special thanks to Warren J. Gore for his support on aircraft preparation and measurement. We are also grateful for comments and suggestions from Benjamin J. Moore and R. Bradley Pierce of NOAA. We appreciate the NOAA ESRL PSD wind profiler data and plots from <https://www.esrl.noaa.gov/psd/data/obs/datadisplay/>. Funding was provided by the NASA Postdoctoral Program, the Bay Area Environmental Research Institute, Science and Technology Corporation, and Scripps Institution of Oceanography, University of California San Diego. This research was also partly supported by the NASA Office of Education's Minority University Research and Education Project (MUREP) Institutional Research Opportunity (MIRO) Contract NNX15AQ02A. The second author is supported by NASA MUREP (NNX15AQ02A), and the Center for Applied Atmospheric Research and Education (CAARE) at San Jose State University (SJSU). Funding for instrumentation and aircraft integration is gratefully acknowledged from Ames Research Center Director's funds. The views, opinions, and findings contained in this report are those of the author(s) and should not be construed as an official National Oceanic and Atmospheric Administration or U.S. Government position, policy, or decision. Resources supporting this work were provided by the NASA High-End Computing (HEC) Program through the NASA Advanced Supercomputing (NAS) Division at NASA Ames Research Center and the NASA Center for Climate simulation (NCCS). We thank the editor and

anonymous reviewers for their very thorough and valuable comments that have helped the authors to significantly improve the manuscript.

REFERENCES

- Bell, G. D., and L. F. Bosart, 1988: Appalachian cold-air damming. *Mon. Wea. Rev.*, **116**, 137–161, [https://doi.org/10.1175/1520-0493\(1988\)116<0137:ACAD>2.0.CO;2](https://doi.org/10.1175/1520-0493(1988)116<0137:ACAD>2.0.CO;2).
- Bosilovich, M. G., R. Lucchesi, and M. Suarez, 2016: MERRA-2: File specification. GMAO Office Note 9 (version 1.1), 73 pp., <https://gmao.gsfc.nasa.gov/pubs/docs/Bosilovich785.pdf>.
- Browning, K. A., and C. W. Pardoe, 1973: Structure of low-level jet streams ahead of mid-latitude cold fronts. *Quart. J. Roy. Meteor. Soc.*, **99**, 619–638, <https://doi.org/10.1002/qj.49709942204>.
- Chen, W.-D., and R. B. Smith, 1987: Blocking and deflection of airflow by the Alps. *Mon. Wea. Rev.*, **115**, 2578–2597, [https://doi.org/10.1175/1520-0493\(1987\)115<2578:BADOAB>2.0.CO;2](https://doi.org/10.1175/1520-0493(1987)115<2578:BADOAB>2.0.CO;2).
- Chou, M. D., and M. J. Suarez, 1994: An efficient thermal infrared radiation parameterization for use in general circulation models. NASA Tech. Memo. 104606, Vol. 3, 85 pp., <https://ntrs.nasa.gov/search.jsp?R=19950009331>.
- Colle, B., and C. F. Mass, 1995: The structure and evolution of cold surges east of the rocky mountains. *Mon. Wea. Rev.*, **123**, 2577–2610, [https://doi.org/10.1175/1520-0493\(1995\)123<2577:TSAEOC>2.0.CO;2](https://doi.org/10.1175/1520-0493(1995)123<2577:TSAEOC>2.0.CO;2).
- , K. A. Loescher, G. S. Young, and N. S. Winstead, 2006: Climatology of barrier jets along the Alaskan coast. Part II: Large-scale and sounding composites. *Mon. Wea. Rev.*, **134**, 454–477, <https://doi.org/10.1175/MWR3038.1>.
- Dettinger, M., 2011: Climate change, atmospheric rivers, and floods in California—A multimodel analysis of storm frequency and magnitude changes. *J. Amer. Water Resour. Assoc.*, **47**, 514–523, <https://doi.org/10.1111/j.1752-1688.2011.00546.x>.
- , F. M. Ralph, T. Das, P. J. Neiman, and D. R. Cayan, 2011: Atmospheric rivers, floods, and the water resources of California. *Water*, **3**, 445–478, <https://doi.org/10.3390/w3020445>.
- Doyle, J. D., 1997: The influence of mesoscale orography on a coastal jet and rainband. *Mon. Wea. Rev.*, **125**, 1465–1488, [https://doi.org/10.1175/1520-0493\(1997\)125<1465:TIOMOO>2.0.CO;2](https://doi.org/10.1175/1520-0493(1997)125<1465:TIOMOO>2.0.CO;2).
- , and T. T. Warner, 1993: A three-dimensional numerical investigation of a Carolina coastal low-level jet during GALE IOP 2. *Mon. Wea. Rev.*, **121**, 1030–1047, [https://doi.org/10.1175/1520-0493\(1993\)121<1030:ATDNIO>2.0.CO;2](https://doi.org/10.1175/1520-0493(1993)121<1030:ATDNIO>2.0.CO;2).
- Durran, D. R., and J. B. Klemp, 1982: On the effects of moisture on the Brunt–Väisälä frequency. *J. Atmos. Sci.*, **39**, 2152–2158, [https://doi.org/10.1175/1520-0469\(1982\)039<2152:OTEOMO>2.0.CO;2](https://doi.org/10.1175/1520-0469(1982)039<2152:OTEOMO>2.0.CO;2).
- Eiserloh, A. J., and S. Chiao, 2015: Modeling studies of landfalling atmospheric rivers and orographic precipitation over northern California. *Meteor. Atmos. Phys.*, **127**, 1–16, <https://doi.org/10.1007/s00703-014-0350-4>.
- Ek, M. B., K. E. Mitchell, Y. Lin, E. Rogers, P. Grunmann, V. Koren, G. Gayno, and J. D. Tarpley, 2003: Implementation of Noah land surface model advances in the National Centers for Environmental Prediction operational mesoscale Eta model. *J. Geophys. Res.*, **103**, 8851, <https://doi.org/10.1029/2002JD003296>.
- Fairlie, T. D., M. A. Avery, R. B. Pierce, J. Al-Saadi, J. Dibb, and G. Sachse, 2007: Impact of multiscale dynamical processes and mixing on the chemical composition of the upper troposphere and lower stratosphere during the Intercontinental Chemical Transport Experiment–North America. *J. Geophys. Res.*, **112**, D16S90, <https://doi.org/10.1029/2006JD007923>.

- Filges, A., C. Gerbig, H. Chen, H. Franke, C. Klaus, and A. Jordan, 2015: The IAGOS-core greenhouse gas package: A measurement system for continuous airborne observations of CO₂, CH₄, H₂O and CO. *Tellus*, **67B**, 27989, <https://doi.org/10.3402/tellusb.v67.27989>.
- Gaines, S. E., S. W. Bowen, R. S. Hipskind, T. P. Bui, and K. R. Chan, 1992: Comparisons of the NASA ER-2 meteorological measurement system with radar tracking and radiosonde data. *J. Atmos. Oceanic Technol.*, **9**, 210–225, [https://doi.org/10.1175/1520-0426\(1992\)009<0210:COTNEM>2.0.CO;2](https://doi.org/10.1175/1520-0426(1992)009<0210:COTNEM>2.0.CO;2).
- Galewsky, J., and A. Sobel, 2005: Moist dynamics and orographic precipitation in northern and central California during the new year's flood of 1997. *Mon. Wea. Rev.*, **133**, 1594–1612, <https://doi.org/10.1175/MWR2943.1>.
- Grell, G. A., J. Dudhia, and D. R. Stauffer, 1994: A description of the fifth generation Penn State/NCAR Mesoscale Model (MM5). NCAR Tech. Note NCAR/TN-398+STR, 121 pp., <https://doi.org/10.5065/D60Z716B>.
- Gill, A. E., 1982: *Atmosphere–Ocean Dynamics*. Academic Press, 662 pp.
- Guan, B., N. P. Molotch, D. E. Waliser, E. J. Fetzer, and P. J. Neiman, 2013: The 2010/2011 snow season in California's Sierra Nevada: Role of atmospheric rivers and modes of large-scale variability. *Water Resour. Res.*, **49**, 6731–6743, <https://doi.org/10.1002/wrcr.20537>.
- Hamill, P., L. T. Iraci, E. L. Yates, W. Gore, T. P. Bui, T. Tanaka, and M. Loewenstein, 2016: A new instrumented airborne platform for atmospheric research. *Bull. Amer. Meteor. Soc.*, **97**, 397–404, <https://doi.org/10.1175/BAMS-D-14-00241.1>.
- Haynes, P. H., 1990: *High-Resolution Three-Dimensional Modeling of Stratospheric Flows: Quasi-Two-Dimensional Turbulence Dominated by a Single Vortex, Topological Fluid Mechanics*. Cambridge University Press, 345–354.
- Hong, S. Y., Y. Noh, and J. Dudhia, 2006: A new vertical diffusion package with an explicit treatment of entrainment processes. *Mon. Wea. Rev.*, **134**, 2318–2341, <https://doi.org/10.1175/MWR3199.1>.
- Houze, R. A., Jr., and S. Medina, 2005: Turbulence as a mechanism for orographic precipitation enhancement. *J. Atmos. Sci.*, **62**, 3599–3623, <https://doi.org/10.1175/JAS3555.1>.
- Hughes, M., A. Hall, and R. G. Fovell, 2009: Blocking in areas of complex topography, and its influence on rainfall distribution. *J. Atmos. Sci.*, **66**, 508–518, <https://doi.org/10.1175/2008JAS2689.1>.
- Jankov, I., P. J. Schultz, C. J. Anderson, and S. E. Koch, 2007: The impact of different physical parameterizations and their interactions on cold season QPF in the American River Basin. *J. Hydrometeor.*, **8**, 1141–1151, <https://doi.org/10.1175/JHM630.1>.
- Kim, J., and H.-S. Kang, 2007: The impact of the Sierra Nevada on low-level winds and water vapor transport. *J. Hydrometeor.*, **8**, 790–804, <https://doi.org/10.1175/JHM599.1>.
- Loescher, K. A., G. S. Young, B. A. Colle, and N. S. Winstead, 2006: Climatology of barrier jets along the Alaskan coast. Part I: Spatial and temporal distributions. *Mon. Wea. Rev.*, **134**, 437–453, <https://doi.org/10.1175/MWR3037.1>.
- Luna-Niño, R., and T. Cavazos, 2018: Formation of a coastal barrier jet in the Gulf of Mexico due to the interaction of cold fronts with the Sierra Madre Oriental mountain range. *Quart. J. Roy. Meteor. Soc.*, **144**, 115–128, <https://doi.org/10.1002/QJ.3188>.
- Martin, A., F. M. Ralph, R. Demirdjian, L. DeHaan, R. Weihs, J. Helly, D. Reynolds, and S. Iacobellis, 2018: Evaluation of atmospheric river predictions by the WRF model using aircraft and regional mesonet observations of orographic precipitation and its forcing. *J. Hydrometeor.*, **19**, 1097–1113, <https://doi.org/10.1175/JHM-D-17-0098.1>.
- Mass, C. F., S. Businger, M. D. Albright, and Z. A. Tucker, 1995: A windstorm in the lee of a gap in a coastal mountain barrier. *Mon. Wea. Rev.*, **123**, 315–331, [https://doi.org/10.1175/1520-0493\(1995\)123<0315:AWITLO>2.0.CO;2](https://doi.org/10.1175/1520-0493(1995)123<0315:AWITLO>2.0.CO;2).
- Mlawer, E. J., S. J. Taubman, P. D. Brown, M. J. Iacono, and S. A. Clough, 1997: Radiative transfer for inhomogeneous atmospheres: RRTM, a validated correlated-k model for the longwave. *J. Geophys. Res.*, **102**, 16 663–16 682, <https://doi.org/10.1029/97JD00237>.
- Neiman, P. J., F. M. Ralph, A. B. White, D. E. Kingsmill, and P. O. G. Persson, 2002: The statistical relationship between upslope flow and rainfall in California's coastal mountains: Observations during CALJET. *Mon. Wea. Rev.*, **130**, 1468–1492, [https://doi.org/10.1175/1520-0493\(2002\)130<1468:TSRBUF>2.0.CO;2](https://doi.org/10.1175/1520-0493(2002)130<1468:TSRBUF>2.0.CO;2).
- , —, —, D. Parrish, J. S. Holloway, and D. L. Bartels, 2006: A multiwinter analysis of channeled flow through a prominent gap along the northern California coast during CALJET and PACJET. *Mon. Wea. Rev.*, **134**, 1815–1841, <https://doi.org/10.1175/MWR3148.1>.
- , —, —, G. A. Wick, J. D. Lundquist, and M. D. Dettinger, 2008: Meteorological characteristics and overland precipitation impacts of atmospheric rivers affecting the west coast of North America based on eight years of SSM/I satellite observations. *J. Hydrometeor.*, **9**, 22–47, <https://doi.org/10.1175/2007JHM855.1>.
- , E. M. Sukovich, F. M. Ralph, and M. Hughes, 2010: A seven-year wind profiler-based climatology of the windward barrier jet along California's northern Sierra Nevada. *Mon. Wea. Rev.*, **138**, 1206–1233, <https://doi.org/10.1175/2009MWR3170.1>.
- , M. Hughes, B. J. Moore, F. M. Ralph, and E. M. Sukovich, 2013: Sierra barrier jets, atmospheric rivers, and precipitation characteristics in northern California: A composite perspective based on a network of wind profilers. *Mon. Wea. Rev.*, **141**, 4211–4233, <https://doi.org/10.1175/MWR-D-13-00112.1>.
- , F. M. Ralph, B. J. Moore, and R. J. Zamora, 2014: The regional influence of an intense sierra barrier jet and landfalling atmospheric river on orographic precipitation in northern California: A case study. *J. Hydrometeor.*, **140**, 358–378, <https://doi.org/10.1175/JHM-D-13-0183.1>.
- Nelson, B. R., O. P. Prat, D.-J. Seo, and E. Habib, 2016: Assessment and implications of NCEP Stage IV quantitative precipitation estimates for product intercomparisons. *Wea. Forecasting*, **31**, 371–394, <https://doi.org/10.1175/WAF-D-14-00112.1>.
- Olson, J. B., B. A. Colle, N. A. Bond, and N. Winstead, 2007: A comparison of two coastal barrier jet events along the southeast Alaskan coast during the SARJET field experiment. *Mon. Wea. Rev.*, **135**, 2973–2994, <https://doi.org/10.1175/MWR3448.1>.
- Parish, T. R., 1982: Barrier winds along the Sierra Nevada mountains. *J. Appl. Meteor.*, **21**, 925–930, [https://doi.org/10.1175/1520-0450\(1982\)021<0925:BWATSN>2.0.CO;2](https://doi.org/10.1175/1520-0450(1982)021<0925:BWATSN>2.0.CO;2).
- Pierrehumbert, R. T., and B. Wyman, 1985: Upstream effects of mesoscale mountains. *J. Atmos. Sci.*, **42**, 977–1003, [https://doi.org/10.1175/1520-0469\(1985\)042<0977:UEOMM>2.0.CO;2](https://doi.org/10.1175/1520-0469(1985)042<0977:UEOMM>2.0.CO;2).
- Ralph, F. M., P. J. Neiman, and G. A. Wick, 2004: Satellite and CALJET aircraft observations of atmospheric rivers over the eastern North Pacific Ocean during the El Niño winter of 1997/98. *Mon. Wea. Rev.*, **132**, 1721–1745, [https://doi.org/10.1175/1520-0493\(2004\)132<1721:SACAOO>2.0.CO;2](https://doi.org/10.1175/1520-0493(2004)132<1721:SACAOO>2.0.CO;2).
- , —, and R. Rotunno, 2005a: Dropsonde observations in low-level jets over the northeastern Pacific Ocean from

- CALJET-1998 and PACJET-2001: Mean vertical-profile and atmospheric-river characteristics. *Mon. Wea. Rev.*, **133**, 889–910, <https://doi.org/10.1175/MWR2896.1>.
- , and Coauthors, 2005b: Improving short-term (0–48 h) cool season quantitative precipitation forecasting: Recommendations from a USWRP workshop. *Bull. Amer. Meteor. Soc.*, **86**, 1619–1632, <https://doi.org/10.1175/BAMS-86-11-1619>.
- , P. J. Neiman, G. A. Wick, S. I. Gutman, M. D. Dettinger, D. R. Cayan, and A. B. White, 2006: Flooding on California's Russian River: The role of atmospheric rivers. *Geophys. Res. Lett.*, **33**, L13801, <https://doi.org/10.1029/2006GL026689>.
- Rutz, J. J., W. J. Steenburgh, and F. M. Ralph, 2014: Climatological characteristics of atmospheric rivers and their inland penetration over the western United States. *Mon. Wea. Rev.*, **142**, 905–921, <https://doi.org/10.1175/MWR-D-13-00168.1>.
- Ryoo, J.-M., D. E. Waliser, D. W. Waugh, S. Wong, E. J. Fetzer, and I. Fung, 2015: Classification of atmospheric river events on the U.S. West Coast using a trajectory model. *J. Geophys. Res. Atmos.*, **120**, 3007–3028, <https://doi.org/10.1002/2014JD022023>.
- Scott, S. G., T. P. Bui, K. R. Chan, and S. W. Bowen, 1990: The meteorological measurement system on the NASA ER-2 aircraft. *J. Atmos. Ocean. Tech.*, **7**, 525–540, [https://doi.org/10.1175/1520-0426\(1990\)007<0525:TMMSOT>2.0.CO;2](https://doi.org/10.1175/1520-0426(1990)007<0525:TMMSOT>2.0.CO;2).
- Skamarock, W. C., and Coauthors, 2008: A description of the Advanced Research WRF version 3. NCAR Tech. Note NCAR/TN-475+STR, 113 pp., <https://doi.org/10.5065/D68S4MVH>.
- Smalley, M., T. L'Ecuyer, M. Lebsack, and J. Haynes, 2014: A comparison of precipitation occurrence from the NCEP Stage IV QPE product and the CloudSat cloud profiling radar. *J. Hydrometeor.*, **15**, 444–458, <https://doi.org/10.1175/JHM-D-13-048.1>.
- Steenburgh, W. J., D. M. Schultz, and B. A. Colle, 1998: The structure and evolution of gap outflow over the gulf of tehuantepec, Mexico. *Mon. Wea. Rev.*, **126**, 2673–2691, [https://doi.org/10.1175/1520-0493\(1998\)126<2673:TSAEOG>2.0.CO;2](https://doi.org/10.1175/1520-0493(1998)126<2673:TSAEOG>2.0.CO;2).
- Strangeways, I. C., 1996: Back to basics: The 'met. Enclosure': Part 2(b)—Raingauges, their errors. *Weather*, **51**, 298–303, <https://doi.org/10.1002/j.1477-8696.1996.tb06230.x>.
- Thompson, G., R. M. Rasmussen, and K. Manning, 2004: Explicit forecasts of winter precipitation using an improved bulk microphysics scheme. Part I: Description and sensitivity analysis. *Mon. Wea. Rev.*, **132**, 519–542, [https://doi.org/10.1175/1520-0493\(2004\)132<0519:EFOWP>2.0.CO;2](https://doi.org/10.1175/1520-0493(2004)132<0519:EFOWP>2.0.CO;2).
- Valenzuela, R., and D. E. Kingsmill, 2015: Orographic precipitation forcing along the coast of Northern California during a landfalling winter storm. *Mon. Wea. Rev.*, **143**, 3570–3590, <https://doi.org/10.1175/MWR-D-14-00365.1>.
- , and —, 2017: Terrain-trapped airflows and orographic rainfall along the coast of northern California. Part I: Kinematic characterization using a wind profiling radar. *Mon. Wea. Rev.*, **145**, 2993–3008, <https://doi.org/10.1175/MWR-D-16-0484.1>.
- , and —, 2018: Terrain-trapped Airflows and Orographic Rainfall along the Cost of Northern California. Part II: Horizontal and vertical structures observed by a scanning Doppler radar. *Mon. Wea. Rev.*, **146**, 2381–2402, <https://doi.org/10.1175/MWR-D-17-0227.1>.
- White, A. B., and Coauthors, 2013: A twenty-first-century California observing network for monitoring extreme weather events. *J. Atmos. Oceanic Technol.*, **30**, 1585–1603, <https://doi.org/10.1175/JTECH-D-12-00217.1>.
- Wick, G. A., P. J. Neiman, and F. M. Ralph, 2013a: Description and validation of an automated objective technique for identification and characterization of the integrated water vapor signature of atmospheric rivers. *IEEE Trans. Geosci. Remote Sens.*, **51**, 2166–2176, <https://doi.org/10.1109/TGRS.2012.2211024>.
- , —, —, and T. M. Hamill, 2013b: Evaluation of forecasts of the water vapor signature of atmospheric rivers in operational numerical weather prediction models. *Wea. Forecasting*, **28**, 1337–1352, <https://doi.org/10.1175/WAF-D-13-00025.1>.
- Yu, C.-K., and B. F. Smull, 2000: Airborne observations of a landfalling cold front upstream of steep coastal orography. *Mon. Wea. Rev.*, **128**, 1577–1603, [https://doi.org/10.1175/1520-0493\(2000\)128<1577:ADOOAL>2.0.CO;2](https://doi.org/10.1175/1520-0493(2000)128<1577:ADOOAL>2.0.CO;2).
- Zhu, Y., and R. E. Newell, 1994: Atmospheric rivers and bombs. *Geophys. Res. Lett.*, **21**, 1999–2002, <https://doi.org/10.1029/94GL01710>.
- , and —, 1998: A proposed algorithm for moisture fluxes from atmospheric rivers. *Mon. Wea. Rev.*, **126**, 725–735, [https://doi.org/10.1175/1520-0493\(1998\)126<0725:APAFMF>2.0.CO;2](https://doi.org/10.1175/1520-0493(1998)126<0725:APAFMF>2.0.CO;2).